

UC Berkeley

UC Berkeley Previously Published Works

Title

Structural mechanism of bridge RNA-guided recombination.

Permalink

<https://escholarship.org/uc/item/8937v940>

Journal

Nature: New biology, 630(8018)

ISSN

0028-0836

Authors

Hiraizumi, Masahiro

Perry, Nicholas

Durrant, Matthew

et al.

Publication Date

2024-06-01

DOI

10.1038/s41586-024-07570-2

Peer reviewed

Structural mechanism of bridge RNA-guided recombination

<https://doi.org/10.1038/s41586-024-07570-2>

Received: 27 November 2023

Accepted: 15 May 2024

Published online: 26 June 2024

Open access

 Check for updates

Masahiro Hiraizumi¹, Nicholas T. Perry^{2,3,4}, Matthew G. Durrant², Teppei Soma¹, Naoto Nagahata¹, Sae Okazaki⁵, Januka S. Athukoralage², Yukari Isayama⁵, James J. Pai², April Pawluk², Silvana Konermann^{2,6}, Keitaro Yamashita⁵, Patrick D. Hsu^{2,3,7}✉ & Hiroshi Nishimasu^{1,5,8}✉

Insertion sequence (IS) elements are the simplest autonomous transposable elements found in prokaryotic genomes¹. We recently discovered that IS110 family elements encode a recombinase and a non-coding bridge RNA (bRNA) that confers modular specificity for target DNA and donor DNA through two programmable loops². Here we report the cryo-electron microscopy structures of the IS110 recombinase in complex with its bRNA, target DNA and donor DNA in three different stages of the recombination reaction cycle. The IS110 synaptic complex comprises two recombinase dimers, one of which houses the target-binding loop of the bRNA and binds to target DNA, whereas the other coordinates the bRNA donor-binding loop and donor DNA. We uncovered the formation of a composite RuvC–Tnp active site that spans the two dimers, positioning the catalytic serine residues adjacent to the recombination sites in both target and donor DNA. A comparison of the three structures revealed that (1) the top strands of target and donor DNA are cleaved at the composite active sites to form covalent 5′-phosphoserine intermediates, (2) the cleaved DNA strands are exchanged and religated to create a Holliday junction intermediate, and (3) this intermediate is subsequently resolved by cleavage of the bottom strands. Overall, this study reveals the mechanism by which a bispecific RNA confers target and donor DNA specificity to IS110 recombinases for programmable DNA recombination.

Transposable elements are mobile DNA sequences that can move or copy themselves to new locations within genomes. They are widespread throughout all domains of life and have vital roles in shaping genome function and evolution³. Transposons typically encode a transposase gene and terminal inverted repeats at both ends of the elements. Using diverse catalytic mechanisms, these transposases recognize the inverted repeats to catalyse the excision and insertion of the transposable element into new target sites in the genome⁴.

Insertion sequence elements are the simplest autonomous transposable elements found in prokaryotic genomes and are classified into approximately 30 families¹. Typical insertion sequence elements are excised and then randomly inserted into new genomic loci by the actions of their cognate transposases. By contrast, the IS110 family elements are excised as circular double-stranded DNA intermediates and then inserted into specific DNA target sequences through unknown mechanisms^{5–10} (Fig. 1a and Extended Data Fig. 1a). Given the conservative transposition cycle of IS110 elements, their encoded transposases can be referred to as recombinases, reflecting a closer functional resemblance to site-specific recombinases such as Bxb1 and Cre^{11,12}. IS110 family elements consist of a left end, a recombinase-coding sequence and a right end, flanked by the CT (cytosine–thymine) core dinucleotide sequences (Fig. 1a and Extended Data Fig. 1a), and unlike

most other insertion sequence elements, they do not encode long terminal inverted repeat sequences, further obscuring their transposition mechanism. Consistent with these unique features of the IS110 elements, the IS110 recombinases differ from other known enzymes and comprise a RuvC-like domain (Pfam PF01548, hereafter referred to as RuvC for simplicity) with a DEDD motif⁷, as well as a Tnp domain (Pfam PF02371) with a conserved serine residue² (Fig. 1b and Supplementary Fig. 1). These sequence features and functional observations indicate that IS110 elements use a distinctive mechanism of action that has, until now, remained elusive.

In our accompanying study², we established that the *Escherichia coli* IS621 element⁷, a member of the IS110 family, reconstitutes a σ^{70} -like promoter at the right–left end junction in its circular intermediate form to express a bRNA from the left end (Fig. 1a and Extended Data Fig. 1a). This bRNA encodes specificity determinants for both donor DNA (dDNA; the IS621 circular form) and target DNA (tDNA; the genomic insertion site) (Fig. 1c and Extended Data Fig. 1a,b). The bRNA target-binding loop (TBL) contains two guide segments: a left target guide (LTG) and a right target guide (RTG), which base pair with the left side of the bottom strand (left target) and the right side of the top strand (right target) of a double-stranded tDNA, respectively (Fig. 1c, Extended Data Fig. 1a,b and Supplementary Fig. 2a). The analogous

¹Department of Chemistry and Biotechnology, Graduate School of Engineering, The University of Tokyo, Tokyo, Japan. ²Arc Institute, Palo Alto, CA, USA. ³Department of Bioengineering, University of California, Berkeley, Berkeley, CA, USA. ⁴San Francisco Graduate Program in Bioengineering, University of California, Berkeley, Berkeley, CA, USA. ⁵Structural Biology Division, Research Center for Advanced Science and Technology, The University of Tokyo, Tokyo, Japan. ⁶Department of Biochemistry, Stanford University School of Medicine, Stanford, CA, USA. ⁷Center for Computational Biology, University of California, Berkeley, Berkeley, CA, USA. ⁸Inamori Research Institute for Science, Kyoto, Japan. ✉e-mail: patrick@arcinstitute.org; nishimasu@g.ecc.u-tokyo.ac.jp

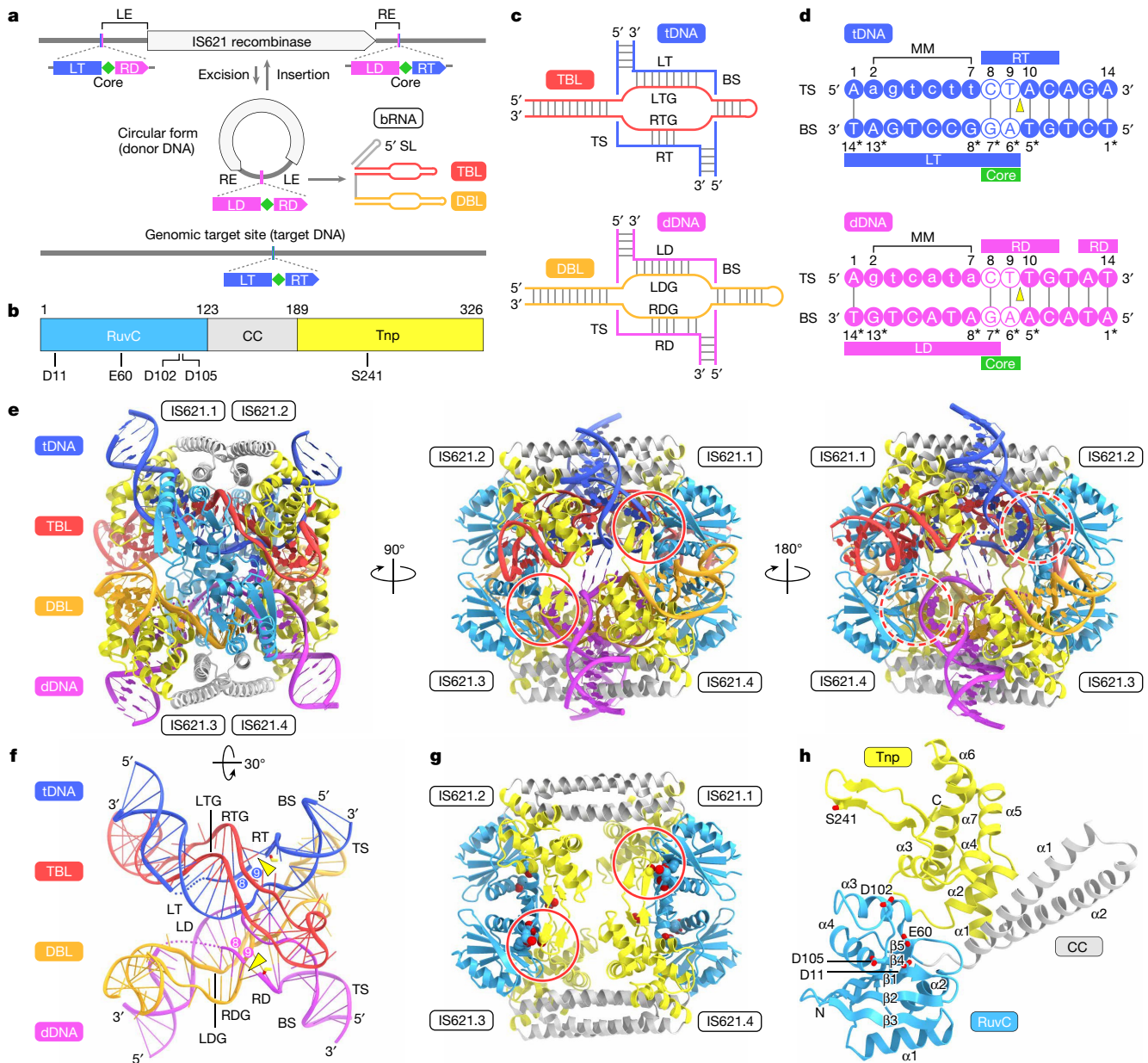


Fig. 1 | IS621 synaptic complex structure. **a**, Schematic of the IS621 insertion sequence element. LD, left donor; RD, right donor; LE, left end; RE, right end, LT, left target; RT, right target; SL, stem loop. **b**, Domain structure of the IS621 recombinase. CC, coiled-coil domain. **c**, Schematics of bRNA-guided dDNA and tDNA recognition. The 5' stem loop and the linker region in the bRNA are omitted, as the TBL and DBL in a single synaptic complex are derived from two different bRNA molecules. BS, bottom strand; TS, top strand. **d**, Nucleotide sequences of the bRNA-complementary regions in the tDNA and dDNA. Mismatched (MM) nucleotides introduced to the top strands for the structural analysis are shown as lowercase letters. Bottom strands are indicated by asterisks. **e, f**, Structures

of the IS621–bRNA–dDNA–tDNA synaptic complex (**e**) and the bRNA–dDNA–tDNA complex (**f**). Disordered regions are indicated by dotted lines, and the CT core dinucleotides (positions 8 and 9) are numbered. In **f**, the S241 residues are shown as stick models. **g, h**, Structures of the tetramer (**g**) and monomer (**h**) of the IS621 recombinase. The catalytic residues are shown as space-filling (**g**) and stick (**h**) models. In **h**, the core α -helices and β -strands in each domain are numbered. In **d, f**, DNA cleavage sites are indicated by yellow triangles. In **e, g**, the active sites with the ordered and disordered S241 residues are indicated by red solid and dashed circles, respectively.

architecture of the donor-binding loop (DBL; composed of a left donor guide (LDG) and a right donor guide (RDG)) base pairs with the left donor and right donor regions of a double-stranded dDNA in a similar manner. Functionally, the IS621 recombinase associates with the bRNA and catalyses recombination between dDNA and tDNA at a central CT core dinucleotide present in both DNA molecules (Fig. 1a and Extended Data Fig. 1a, b). We demonstrated its broad and modular reprogrammability to desired dDNA and tDNA substrates for genome insertion, inversion and excision, laying the groundwork for a unified mechanism for programmable DNA rearrangements². In this study, we solved the

high-resolution cryo-electron microscopy (cryo-EM) structures of the IS621 synaptic complexes in several reaction intermediate states, revealing the bRNA-guided DNA recombination mechanism.

IS621 synaptic complex structure

For cryo-EM analysis, we first attempted to reconstitute the synaptic complex comprising the IS621 recombinase, a full-length 177-nucleotide (nt) bRNA, a 44-base pair (bp) dDNA (the right end–left end junction with the left donor–core–right donor sequence in the circular form)

and a 38-bp tDNA (the genomic insertion site with the left target-core-right target sequence) from the natural IS621 element found in *E. coli* (Fig. 1b,c, Extended Data Fig. 1a,b and Supplementary Fig. 2a). However, the IS621–bRNA complex did not form a stable synaptic complex with dDNA and tDNA on size-exclusion chromatography (Extended Data Fig. 2a). To facilitate bRNA-mediated DNA targeting, we introduced mismatches into the top strand of the dDNA (6 nt) and tDNA (6 nt) at positions 2–7, and found that these mismatches facilitated synaptic complex formation and in vitro DNA recombination (Fig. 1d and Extended Data Figs. 1a,b and 2a,b). Using these mismatch-containing dDNA and tDNA molecules, we determined the cryo-EM structure of the IS621–bRNA–dDNA–tDNA synaptic complex at 2.5 Å resolution (Extended Data Fig. 2c–h).

The synaptic complex consists of four IS621 recombinase protomers (IS621.1–4) and the TBL and DBL modules of the bRNA, as well as tDNA and dDNA (Fig. 1e–g and Supplementary Video 1). The 5' stem loop of the bRNA, as well as the linker region between the TBL and DBL, are not visible in the density map (Extended Data Fig. 2h), suggesting their flexibility. Deletion of the 5' stem loop decreased bRNA binding to the IS621 recombinase (Extended Data Fig. 2i) and slightly reduced IS621-mediated recombination in *E. coli* (Extended Data Fig. 2j), suggesting that the 5' stem loop does not form specific interactions with the recombinase, but rather enhances the IS621–bRNA interaction, possibly through nonspecific RNA backbone interactions. The 5' stem loops are structurally conserved among IS110 orthologues, although their sequences are diverse², suggesting their conserved functional roles. In the structure, the TBL 3' end (C95) and the DBL 5' end (A110) are approximately 80 Å apart (Extended Data Fig. 2k), suggesting that two different bRNA molecules contribute the TBL and DBL, respectively, to a single synaptic complex. Supporting this notion, we observed dimers of the synaptic complex during 2D classification, in which two synaptic complexes are probably held together by two bRNA molecules (Extended Data Fig. 2d).

IS621.1 and IS621.2 form a dimer that interacts with the TBL and tDNA, while IS621.3 and IS621.4 form a dimer that interacts with the DBL and dDNA (Fig. 1e). Consistent with our functional data showing RNA-guided DNA recognition by the IS621 recombinase², the TBL and DBL base pair with tDNA and dDNA, respectively (Fig. 1f). The tDNA and dDNA molecules bend around the central catalytic site, adopting an X-shaped architecture (Fig. 1e,f). Consistent with the observed recombination adjacent to the CT core sequences², both the tDNA (between tT9 and tA10) and the dDNA (between dT9 and dT10) are cleaved adjacent to the CT core sequences (tC8–tT9 and dC8–dT9), with the conserved serine residues (S241) in IS621.4 and IS621.2 forming covalent 5'-phosphoserine linkages with tDNA tA10 and dDNA dT10, respectively (Fig. 1e,f). As observed for serine recombinases¹³, SDS-PAGE analysis of the synaptic complex revealed slower-migrating bands that probably correspond to covalent IS621–DNA complexes (Extended Data Fig. 2a). We conclude that this structure represents the post-top strand cleavage state of the IS621 synaptic complex before the dDNA and tDNA strands are exchanged.

IS621 recombinase structure

The IS621 recombinase consists of a RuvC domain (residues 1–122), a two-stranded α -helical coiled-coil domain (residues 123–188) and a Tnp domain (residues 189–326) (Fig. 1b,h). The RuvC domain adopts an RNase H fold, comprising a five-stranded β -sheet flanked by four α -helices, with an active site formed by the DEDD motif (D11, E60, D102 and D105) (Fig. 1h). Although the RuvC domain of IS621 shares structural similarity to those of other proteins, such as Cas9, the third residue in the DEDD motif (D102 in IS621) is often replaced in other RuvC domains^{14–16} (Extended Data Fig. 3a). The Tnp domain comprises seven α -helices, with the conserved serine residue S241 located in a loop region between helices α 3 and α 4 (Fig. 1h). A Dali search¹⁷ revealed that

the Tnp domain lacks detectable structural similarity with any other known proteins. The coiled-coil domain contains two α -helices and mediates the dimerization between IS621.1 and IS621.2 and between IS621.3 and IS621.4 (Fig. 1g,h).

The four IS621 protomers are structurally similar, except for the D102 loops in the RuvC domains and the S241 loops in the Tnp domains (Extended Data Fig. 3b,c). The S241 loops in IS621.2 and IS621.4 are ordered and interact with the D102 loops in IS621.3 and IS621.1, respectively, forming composite active sites that span between the two distinct dimers in the synaptic complex (Fig. 1g and Extended Data Fig. 3d). By contrast, the S241 loops in IS621.1 and IS621.3 are disordered, with the D102 loops in IS621.2 and IS621.4 adopting distinct conformations from those in IS621.1 and IS621.3 (Extended Data Fig. 3b,c). Whereas typical RuvC-like domains do not require other domains for their catalytic activity, the RuvC domains of the IS110 recombinases function together with their Tnp domains, with the third residue in the IS110-specific DEDD motif (D102 in IS621) forming a composite active site with S241 of the IS110-specific Tnp domain. This distinctive arrangement of the catalytic residues probably helps to connect the two dimers in the synaptic complex and prevent DNA cleavage from occurring before synaptic complex formation.

bRNA architecture

Our structure reveals how the target-binding and donor-binding modules of the bRNA confer DNA specificity to the IS621 ribonucleoprotein complex. The TBL (nucleotides 34–98) comprises stem, LTG, stem loop and RTG regions, which are connected by four linker regions (C47–U49, U59, G72–U73 and U83–U86), whereas the DBL (nucleotides 110–177) similarly comprises stem, LDG, stem loop and RDG regions connected by four linker regions (G121–G122, A131–U132, G155–U156 and U168) (Fig. 2a–c and Supplementary Fig. 2a). The TBL and DBL adopt similar pseudo-symmetric structures with common features, such as flipped-out A nucleotides (A43 and A67 in TBL and A116 and A150 in DBL) and G nucleotides with the *syn* conformation (G48 and G72 in TBL and G121 and G155 in DBL) (Fig. 2a–c and Supplementary Fig. 2b). These A and G nucleotides are highly conserved among the IS110 family elements² and are similarly recognized by the Tnp domains in the four IS621 protomers (Extended Data Fig. 4 and Supplementary Fig. 2c,d). The TBL and DBL also interact with the IS621 recombinase via sugar-phosphate backbone contacts (Extended Data Fig. 4). These structural findings revealed how the IS621 recombinase dimers associate with the structurally distinct TBL and DBL to form two similar ribonucleoprotein complexes.

DNA recognition mechanism

As predicted by our covariation analysis between bRNA and tDNA–dDNA², LTG (A50–U58) and RTG (G77–G80) in the TBL form base pairs with tT14*–tA6* and tC11–tC8 in the tDNA, respectively, whereas LDG (A123–C130) and RDG (A157–U158/C162–G165) in the DBL form base pairs with dT14*–dG7* and dT14–dA13/dG11–dC8 in the dDNA, respectively (Fig. 2a–c and Extended Data Figs. 4 and 5a,b). We noticed the formation of non-canonical base pairs between TBL G53 and tDNA tT11* and between DBL G161 and dDNA dT12. U159 and U160 are flipped out from the RDG–right donor heteroduplex, with U159 forming a base pair with A131 (Fig. 2a,c). Consistent with our computational and functional analyses², these structural findings demonstrate that the LTG and RTG in the TBL, and the LDG and RDG in the DBL, recognize the bottom and top strands of tDNA and dDNA, respectively, through a unique base-pairing scheme.

The IS621 element and related orthologues contain highly conserved CT core dinucleotides at both ends, and the IS621 recombinase preferentially catalyses recombination between dDNA and tDNA molecules containing the CT core dinucleotide². Whereas the second T nucleotide

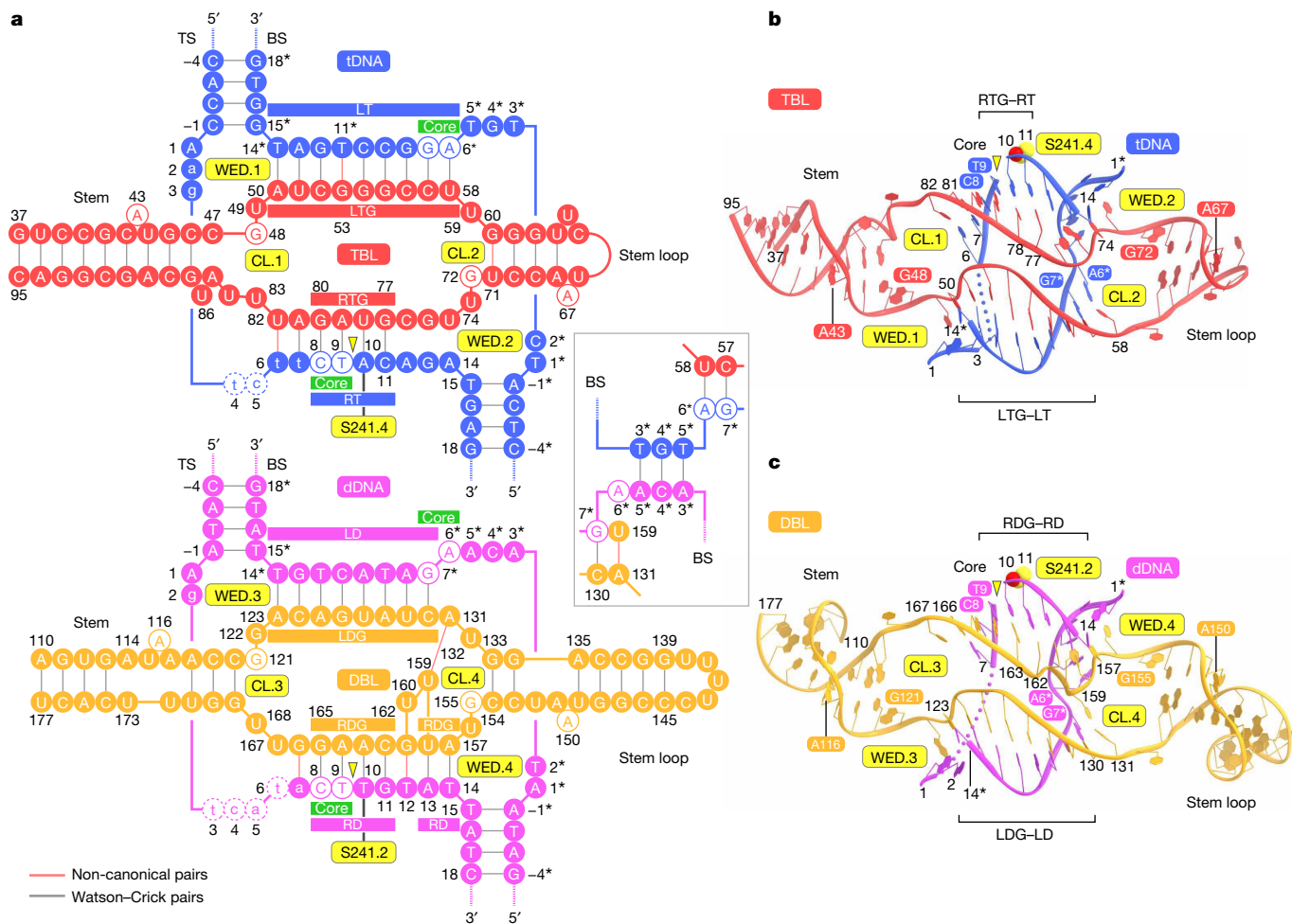


Fig. 2 | bRNA architecture. **a**, Schematics showing base pairing between the bRNA and tDNA (top) and bRNA and dDNA (bottom). The covalent 5'-phosphoserine–DNA linkages are indicated by grey lines. Non-canonical base pairing is indicated by red lines. Disordered nucleotides are indicated by dashed circles. The 5' stem loop and the linker region are omitted. CL, catalytic

loop; WED, hydrophobic wedge. **b,c**, Structures of TBL–tDNA (**b**) and DBL–dDNA (**c**). Disordered regions are indicated by dotted lines. The S241 residues are depicted as space-filling models. In **a–c**, DNA cleavage sites are indicated by yellow triangles.

is almost invariant, the first C nucleotide is less conserved. Indeed, the GT, AT and TT core sequences also supported IS621-mediated recombination in *E. coli* cells². Our structure explains the preference of the IS621 recombinase for the CT core dinucleotides. The tT9 and dT9 nucleobases in the CT cores of tDNA and dDNA are recognized by the main-chain amide group of G63 in the RuvC.1 and RuvC.3 domains, respectively, explaining the stricter conservation of a T nucleotide at position 9 (Extended Data Figs. 4 and 5c,d). Although the tC8 and dC8 nucleobases in the CT core do not contact the protein, the G80 (RTG) and G165 (RDG) nucleobases form hydrogen bonds with the main-chain carbonyl group of A61 in the RuvC.1 and RuvC.3 domains, respectively. Meanwhile, their complementary tG7* and dG7* nucleobases are recognized by the N84 residue in the RuvC.2 and RuvC.4 domains, respectively (Extended Data Figs. 4 and 5e,f). Modelling of G at position 8 in the tDNA and dDNA suggested that the G nucleobase at this position can form hydrogen bonds with the main-chain carbonyl group of A61, whereas A or T at position 8 would be incapable of this interaction (Extended Data Fig. 5g), consistent with the preference of IS621 for C/G over A/T at the first position in the core dinucleotide². Together, these findings explain the core dinucleotide preference of the IS621 recombinase.

Our structure also reveals how the Tnp domains destabilize the DNA duplexes to promote bRNA-mediated recognition of both tDNA and dDNA. Y264, M265 and M268 in the Tnp.1 and 2 and Tnp.3 and 4 domains

wedge between the tA1–tT14* and tA14–tT1* pairs in tDNA and between the dA1–dT14* and dT14–dA1* pairs in dDNA, respectively (Extended Data Figs. 4 and 5h). Mutations of these three residues substantially reduced the IS621-mediated recombination in *E. coli* (Extended Data Fig. 5i,j), confirming the functional importance of the hydrophobic wedge. Hydrophobic residues are quite common at these three positions among IS110 orthologues (Supplementary Fig. 1), suggesting that the hydrophobic wedge is a conserved feature of the IS110 recombinases.

Synaptic complex formation

The IS621 synaptic complex appears to result from the assembly of the two IS621.1/2–TBL–tDNA and IS621.3/4–DBL–dDNA dimeric complexes (Fig. 3a,b). The RuvC domains have a primary role in synaptic complex formation, with the two dimers contacting each other through RuvC–RuvC interactions (Fig. 3c,d and Supplementary Video 2). As described above, the S241 loops in Tnp.4 and Tnp.2 penetrate the DBL and TBL to interact with the D102 loops in RuvC.1 and RuvC.3, respectively, thereby forming the composite active sites comprising D11, E60 and D105 (RuvC) and S241 (Tnp) (Fig. 3c,d and Supplementary Video 2). The D102 residues from RuvC.1 and RuvC.3 form hydrogen bonds with the conserved G242 residues of Tnp.4 and Tnp.2 to stabilize the conformation of the S241 loops (Extended Data Fig. 6a). In contrast to this physical proximity and interaction between RuvC.1 and Tnp.4

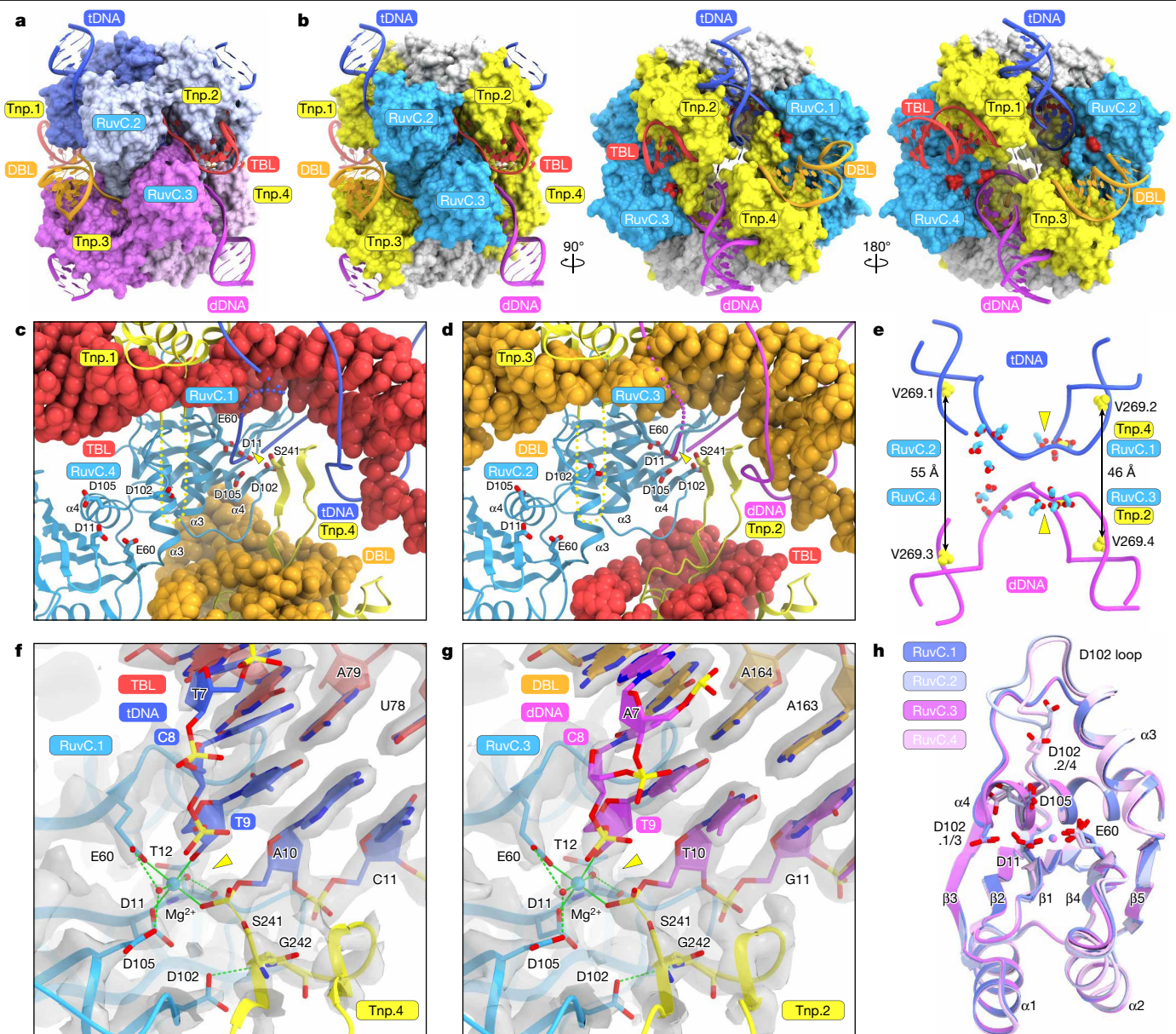


Fig. 3 | Synaptic complex formation. **a, b**, Surface representations of the IS621 synaptic complex, coloured according to the protomers (**a**) and domains (**b**). In **b**, the catalytic residues are coloured in red. **c, d**, Active sites formed by RuvC.1 and Tnp.4 (**c**) and RuvC.3 and Tnp.2 (**d**). The TBL and DBL are shown as space-filling models. DNA cleavage sites are indicated by yellow triangles. Disordered regions are indicated by dotted lines. **e**, Locations of the active sites relative to the tDNA and dDNA. **f, g**, Close-up views of the active sites formed by RuvC.1

and Tnp.4 (**f**) and RuvC.3 and Tnp.2 (**g**). Cryo-EM density maps are shown as grey semi-transparent surfaces. The Mg^{2+} ions and water molecules are depicted as cyan and red spheres, respectively. Hydrogen and coordinate bonds are shown as green dashed and solid lines, respectively. DNA cleavage sites are indicated by yellow triangles. **h**, Superimposition of the RuvC domains in the four IS621 protomers. The Mg^{2+} ions are depicted as spheres.

and between RuvC.3 and Tnp.2, the other two Tnp domains are farther away from their respective RuvC partners, rendering their S241 loops incapable of forming the same kind of composite active site (Fig. 3c–e).

The synaptic complex is further stabilized by the interaction between the stem loop of the DBL (DBL-SL) and RuvC.1 (Extended Data Fig. 6b). U142, U143 and C144 in DBL-SL form base-specific contacts with T30, H28 and R27 in RuvC.1, respectively (Extended Data Fig. 6c). The replacement of nucleotides 137–147 of DBL-SL with a GAAA tetraloop reduced the *in vitro* recombination activity of the system (Extended Data Fig. 6d), indicating the functional importance of these interactions for synaptic complex assembly. By contrast, the corresponding stem loop of the TBL (TBL-SL) is shorter than DBL-SL and does not contact RuvC.3 (Extended Data Fig. 6b). Separate TBL and DBL molecules similarly supported IS621-mediated recombination *in vitro* (Extended Data Fig. 6e), lending

further confidence to the notion that the TBL and DBL within a single synaptic complex are derived from two distinct bRNA molecules. We observed that tT3*, tG4* and tT5* of the tDNA form base pairs with dA5*, dC4* and dA3* of the dDNA, respectively (Extended Data Fig. 6b,f). However, donor–target base pairing at these positions did not affect recombination efficiencies in our bacterial recombination assays², indicating that these donor–target base pairs are not functionally important.

Given the structural similarity between the IS621.1/2–TBL–tDNA and IS621.3/4–DBL–dDNA dimeric complexes (Supplementary Fig. 3a,b), we wondered whether IS621 can mediate target–target and/or donor–donor recombination. We found that IS621 is capable of donor–donor, but not target–target, recombination *in vitro* (Supplementary Fig. 3c). A model of the IS621–TBL–tDNA tetrameric complex suggests that two IS621–TBL–tDNA dimeric complexes cannot form the tetrameric

synaptic complex, due to the lack of the DBL-SL-RuvC interactions (Supplementary Fig. 3d), thus explaining why IS621 cannot mediate target–target recombination. By contrast, a model of the IS621–DBL–dDNA tetrameric complex indicates that the DBL-SL-RuvC interaction on both constituent dimers may promote synaptic complex formation (Supplementary Fig. 3e), thereby potentially allowing donor–donor recombination². We observed rare instances of donor–donor recombination, but not target–target genomic rearrangements, in *E. coli*², suggesting that the low target–target recombination efficiency of IS621 biologically contributes to preventing unintended genomic rearrangements. Together, our analyses reveal that the IS621 synaptic complex is stabilized by the protein–protein and protein–nucleic acid interactions between the two distinct dimers.

Active site architecture

In the RuvC.1–Tnp.4 composite active site, the top strand of tDNA is cleaved between tT9 and tA10, adjacent to the CT core (tC8–tT9) (Fig. 3f). S241 in Tnp.4 forms a covalent 5′-phosphoserine intermediate with tA10, generating a 3′-OH group on tT9. This 3′-OH group and the phosphate group of tA10–S241.4 are coordinated by a Mg²⁺ ion, which is further coordinated by D11 and E60 in RuvC.1 and two water molecules, which in turn form hydrogen bonds with E60, D105 and T12 in RuvC.1. In the RuvC.2–Tnp.3 active site, the top strand of dDNA is cleaved between dT9 and dA10, thereby generating a 3′-OH group in dT9 and a 5′-phosphoserine intermediate between dA10 and S241.2, which are stabilized by a Mg²⁺ ion bound to RuvC.3 (Fig. 3g). Although D11 and E60 assume similar conformations in all four RuvC domains, D102 and D105 adopt distinct conformations in RuvC.1 and RuvC.3 compared with RuvC.2 and RuvC.4, as the RuvC.1 and RuvC.3 domains neither interact with the S241 loop nor participate in composite active site formation (Fig. 3h). The mutation of D11, E60, D102, D105 or S241 abolished IS621-mediated recombination in our in vitro and bacterial recombination assays (Extended Data Fig. 6g,h), confirming the essential role of the RuvC–Tnp composite active site. Together, these findings revealed that D11, E60, D102 and D105 in the RuvC.1 and RuvC.3 domains and S241 in the opposite Tnp.4 and Tnp.2 domains form the composite active sites that cleave the top strands of tDNA and dDNA adjacent to the CT core, respectively, thereby generating the 5′-phosphoserine intermediates during IS621-catalysed recombination.

Handshake base pairing

The tyrosine recombinase Cre forms a tetrameric synaptic complex with two DNA molecules containing *loxP* sequences and cleaves the top strands of both DNA molecules, forming covalent 3′-phosphotyrosine–DNA linkages and free 5′-OH groups¹². The 5′-OH groups then attack the 3′-phosphotyrosine intermediates in the opposite DNA molecule to achieve top-strand exchange, creating a Holliday junction intermediate that is resolved by cleavage of the bottom strand followed by a second strand exchange to complete the recombination reaction¹². Thus, the 5′-phosphoserine–DNA intermediates that we observed in the IS621 structure suggest that the top strands of tDNA and dDNA are exchanged after cleavage. However, the present structure is trapped in the pre-strand exchange state, probably because strand exchange is prevented due to the base pairs between the TBL/DBL and the mismatched nucleotides that we introduced for cryo-EM analysis (A81:tT7, U82:tT6 and G166:dA7).

Our nucleotide covariation analysis² detected uncharacterized covariation signals indicating base-pairing potential between position 7 of the tDNA and dDNA with their non-cognate bRNA loops across hundreds of IS110 orthologues (that is, position 7 in tDNA and position 7 in dDNA may base pair with position 166 in the RDG and position 81 in the RTG, respectively) (Extended Data Fig. 7a,b). These observations suggest that the formation of new base pairs at these positions

after strand exchange is important for promoting the strand exchange process. We named these nucleobases (positions 81–82 and 166–167 in the bRNA) handshake guides (HSGs), due to their potential role in helping to ‘introduce’ the donor top strand to the TBL and the target top strand to the DBL for top-strand exchange.

To test the effect of handshake base pairing (HSB) on IS621-mediated recombination, we performed in vitro recombination experiments using three bRNAs with different HSG sequences, along with tDNA (with tG6 and tC7) and dDNA (with dA6 and dT7) (Extended Data Fig. 8a). The wild-type (WT) bRNA produced the expected recombination product, but also substantial amounts of cleaved tDNA and dDNA, suggesting that strand exchange was less efficient than top-strand cleavage (Extended Data Fig. 8b). In the second bRNA variant (post-HSB), we extended the RTG–right target complementarity by three additional base pairs (U74:tA14–U76:tA12), which enhanced the recombination efficiency in *E. coli*². In addition, we reprogrammed U167 in the HSG to C, so that the HSGs of the TBL and DBL base pair with positions 6–7 in dDNA and tDNA after strand exchange, respectively (that is, TBL–dDNA and DBL–tDNA non-cognate base pairs). In contrast to the WT bRNA, the post-HSB bRNA strongly supported DNA recombination in vitro and drastically reduced the production of cleaved dDNA (Extended Data Fig. 8b). In the third bRNA variant (pre-HSB), we mutated the HSGs of each binding loop to base pair with their cognate DNA before strand exchange (that is, TBL–tDNA and DBL–dDNA cognate base pairs). The pre-HSB bRNA mediated robust cleavage of the top strands of tDNA and dDNA, but did not lead to productive in vitro recombination (Extended Data Fig. 8b). These results indicate that the base pairing between the HSGs of the TBL and DBL and their non-cognate DNA facilitates strand exchange, whereas the base pairing between the HSGs and their cognate DNA inhibits strand exchange.

Next, we explored whether the potential of the DBL HSG to base pair with tDNA would affect the efficiency of recombination in *E. coli*. Mirroring our results in vitro, we observed that the G166A mutation in the DBL, which enables base pairing to dT7 of the dDNA, dramatically reduced the recombination efficiency, whereas G166 (WT), G166C and G166U allowed functional recombination (Extended Data Fig. 8c). Furthermore, reprogramming U167 to G, which can base pair with tC6 of the tDNA after strand exchange, enhanced the recombination efficiency (approximately 1.2-fold). Together, our in vitro and in cellulo recombination assays revealed that the HSG positions can be programmed as a key determinant of recombination efficiency.

To understand how the pre-HSB bRNA precludes recombination, we determined the cryo-EM structure of the synaptic complex with the pre-HSB bRNA (Supplementary Fig. 4a–d). The structure is similar to our original structure, with the top strands of tDNA and dDNA cleaved to form 5′-phosphoserine intermediates (Supplementary Fig. 4e–h). However, in contrast to the original structure, the HSGs in the TBL and DBL form the expected base pairs with the tDNA and dDNA, respectively, thereby impeding top-strand exchange (Supplementary Fig. 4e–h). Thus, our biochemical and structural observations indicate that the cognate base pairing with the HSGs traps the IS621 synaptic complex in the pre-strand exchange ‘locked’ state and does not allow recombination to proceed. Collectively, these findings strongly support our hypothesis that HSGs, which are conserved in many natural IS110 systems, enable the top strands of both dDNA and tDNA to form base pairs with the opposite bRNA loop, thereby facilitating strand exchange.

Strand exchange mechanism

To explore the next steps of the IS621-catalysed recombination mechanism, we determined the cryo-EM structure of the IS621 synaptic complex containing the post-HSB bRNA with the following features that would facilitate recombination: (1) RTG extension (positions 74–76), in which U74, C75 and U76 in the TBL base pair with tA14, tG13 and tA12 in the tDNA, respectively to stabilize the synaptic complex;

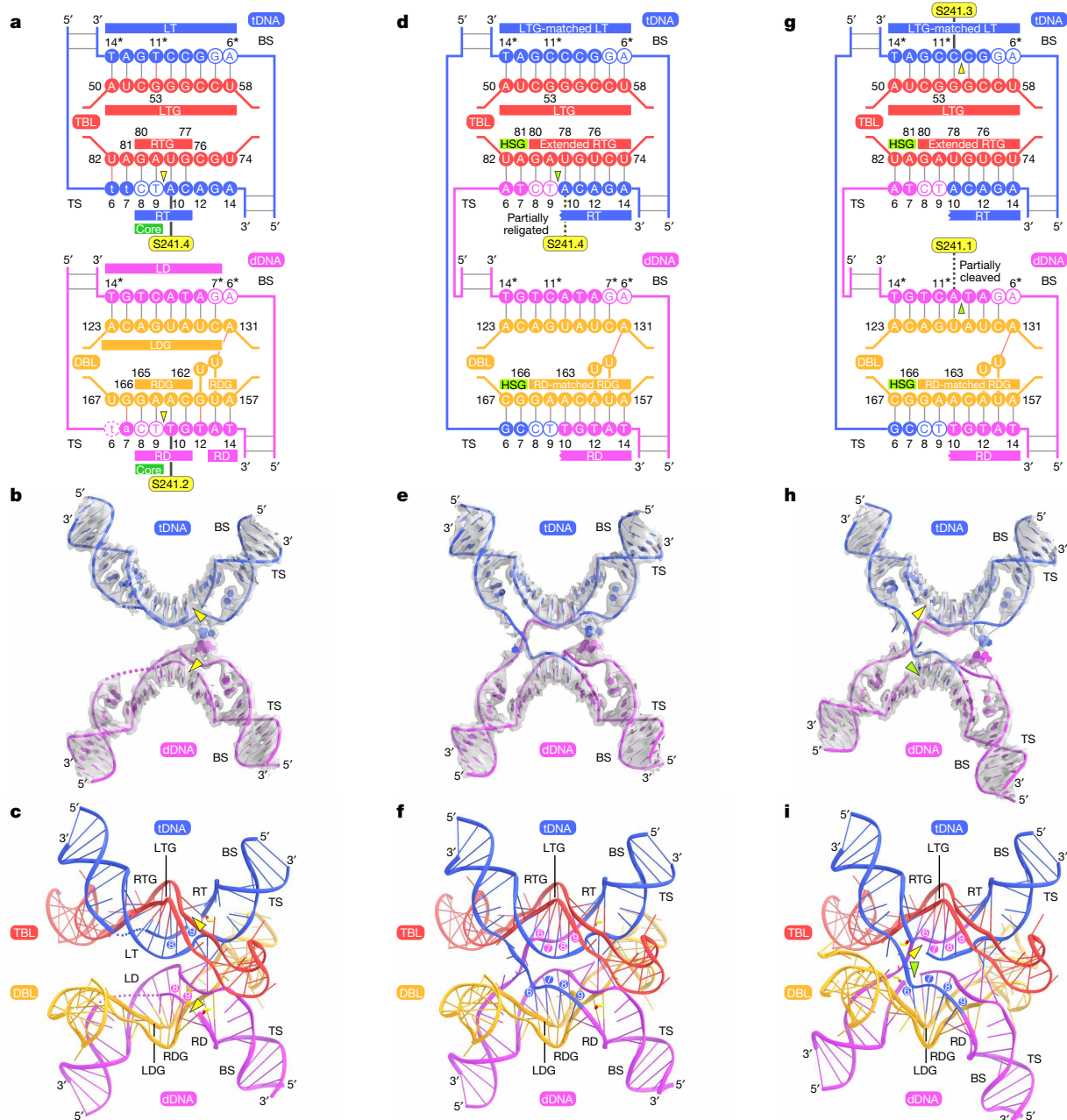


Fig. 4 | Strand exchange mechanism. a–i, Schematics of TBL–tDNA and DBL–dDNA and the structures of tDNA and dDNA, and TBL–tDNA and DBL–dDNA, in the IS621 synaptic complexes in the pre-strand exchange state (the complex with the WT bRNA for comparison) (a–c); the post-strand exchange, Holliday junction intermediate state (state 1) (d–f); and the post-strand exchange,

Holliday junction resolution state (state 2) (g–i). DNA cleavage sites are indicated by yellow triangles, whereas partial cleavage and religation are indicated by green triangles. In b, e, h, cryo-EM density maps are shown as grey semi-transparent surfaces. In b, c, disordered regions are indicated by dotted lines. In c, f, i, positions 6–9 in the dDNA and tDNA are numbered.

(2) replacement of non-canonical base pairs observed in the original structure (positions 53 and 161); and (3) one additional handshake base in the DBL (position 167) (Fig. 4a–i and Supplementary Fig. 5a–g). Our cryo-EM analysis revealed two distinct conformational states: state 1 (2.9 Å resolution) and state 2 (2.7 Å resolution) (Fig. 4d–i, Extended Data Fig. 9a, b and Supplementary Video 3). As expected, in both states 1 and 2, U74–U76 of bRNA base pair with tA14–tA12 of tDNA, whereas G53 and A161 of bRNA form canonical base pairs with tC11* of tDNA and dT12 of dDNA, respectively (Fig. 4d, g). Of note, the top strands of tDNA and dDNA are cleaved downstream of the CT core (between tT9 and tA10 in tDNA and between dT9 and dT10 in dDNA) and then exchanged, resulting in the formation of new TBL–dDNA and DBL–tDNA base pairs, as predicted by our HSG experiments (Fig. 4d–i). The RDG remains

bound to positions 10–14 of the dDNA, while forming new base pairs with the incoming core (tC8–tT9) of the tDNA top strand. Adjacent to this interaction, positions 166–167 of the DBL (the HSG region) also base pair with positions 6–7 of the tDNA. Similarly, the RTG remains bound to positions 10–14 of the tDNA, while forming new base pairs with the incoming core (dC8–dT9) of the dDNA top strand. In addition, positions 81–82 of the TBL (the other HSG region) base pair with positions 6–7 of the dDNA.

In both structures, phosphodiester bonds are formed between dDNA dT9 and tDNA tA10 and between tDNA tT9 and dDNA dT10, with the S241.4 and S241.2 residues dissociated from tDNA tA10 and dDNA dT10, respectively, creating a Holliday junction intermediate (Extended Data Fig. 9c–f). In state 1, the phosphodiester bond between dDNA dT9 and

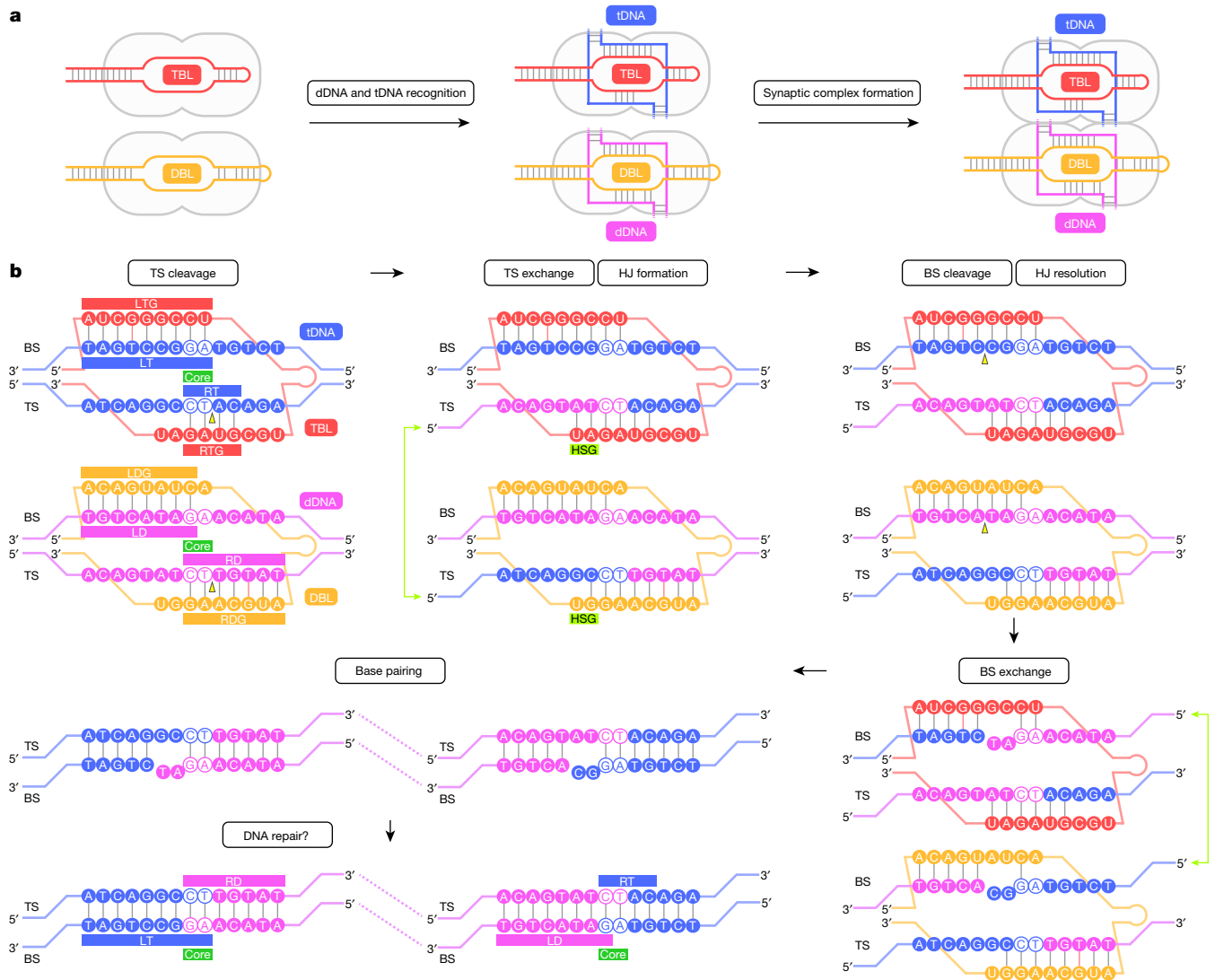


Fig. 5 | Bridge recombination mechanism. a, b, Proposed mechanisms of the IS621 synaptic complex formation (a) and the IS621-mediated DNA recombination (b). Two IS621 recombinase molecules bind to the TBL and DBL from two different bRNA molecules to form the IS621-TBL and IS621-DBL dimeric complexes, respectively. IS621-TBL and IS621-DBL recognize tDNA and dDNA, respectively, and then IS621-TBL-tDNA and IS621-DBL-dDNA form the tetrameric synaptic complex. In the synaptic complex, the top strands of tDNA and dDNA are cleaved at the RuvC-Tnp active sites, with the catalytic S241

residues forming covalent 5'-phosphoserine intermediates. The top strands are then exchanged and religated to form a Holliday junction (HJ) intermediate, which is resolved by the cleavage of the bottom strands at the RuvC-Tnp active sites. It is possible that the bottom strands are exchanged, and mismatched nucleotides are excised and repaired in *E. coli* cells, thereby completing the recombination. DNA cleavage sites are indicated by yellow triangles. Canonical and non-canonical base pairs are indicated by grey and red lines, respectively.

tDNA tA10 exhibits relatively weak density, with S241.4 located close to tDNA tA10 (Extended Data Fig. 9c), suggesting partial religation between dDNA dT9 and tDNA tA10. Together, these observations support the notion that IS621 cleaves the top strands of tDNA and dDNA, followed by strand exchange and religation to form a Holliday junction intermediate.

In state 1, the S241 loops in Tnp.1 and 3 are disordered and the bottom strands of tDNA and dDNA are intact, as in the pre-strand exchange structure (Fig. 4d-f and Extended Data Fig. 9a,g,h). By contrast, in state 2, the S241 loops in Tnp.1 and 3 become ordered and the bottom strands of tDNA and dDNA are cleaved between tC9* and tC10* and between dT9* and dA10* at the RuvC.2-Tnp.3 and RuvC.4-Tnp.1 active sites, with the S241.3 and S241.1 residues covalently linked to tDNA tC10* and dDNA dA10*, respectively (the bottom strand of dDNA is partially cleaved) (Fig. 4g-i and Extended Data Fig. 9b,i,j). Accordingly, the Holliday junction intermediate is resolved by the cleavage of the tDNA and dDNA bottom strands at the RuvC-Tnp

composite active sites of the two IS621 protomers that did not participate in top-strand cleavage (RuvC.2-Tnp.3 and RuvC.4-Tnp.1). We conclude that the IS621 synaptic complex structures in states 1 and 2 represent the post-strand exchange, the Holliday junction intermediate state and the Holliday junction resolution state, respectively. Together, our structural and functional data reveal a step-by-step mechanism explaining how the IS621 recombinase and its bispecific bRNA orchestrate programmable recombination between donor and target DNA.

Discussion

The IS621 recombinase of the IS110 family utilizes a bispecific bRNA with independently programmable target-binding and donor-binding loops to orchestrate recombination between diverse pairs of DNA sequences². Here we provide the first view of this new class of RNA-guided DNA recombinase complexes, illuminating how the IS621

recombinase brings together two bRNA-specified DNA molecules to catalyse their recombination (Fig. 5a,b).

Like site-specific recombinases such as Cre¹², the IS621 recombinase catalyses the recombination reaction consisting of top-strand cleavage and exchange, Holliday junction formation, and bottom-strand cleavage and exchange (Extended Data Fig. 10 and Supplementary Discussion). However, IS621 uses a distinct domain architecture, RuvC–Tnp composite active sites and a bRNA guide, thereby distinguishing it from all known recombinase systems^{3,11,12,18,19} (Supplementary Fig. 6). Although many recent studies have expanded the known universe of RNA-guided enzymes^{20–33}, our discovery of the IS110 bridge RNA illustrates a conceptually distinct way by which enzymes utilize RNA-mediated DNA recognition to manipulate nucleic acids (Supplementary Discussion). Not only does IS621 represent the first example of a single-protein RNA-guided DNA recombinase but its bRNA also contains two distinct guide segments that base pair with both the top and bottom strands of the dDNA and tDNA – a unique feature among all characterized RNA-guided systems to date.

The cryo-EM structures that we determined in this study represent the insertion step in the IS621 transposition cycle, where the circular intermediate (dDNA) recombines into the genomic target site (tDNA). Other stages of the IS621 transposition cycle remain to be mechanistically investigated. Notably, the IS621 system comprises only a single, small protein (326 amino acids) and a single non-coding RNA molecule (177 nt) to accomplish modular and programmable recognition of dDNA and tDNA and their recombination – without introducing double-stranded DNA breaks. Collectively, this work provides fundamental insights into transposable element spreading and RNA-guided enzymatic mechanisms, and offers a mechanistic framework to understand and engineer bridge recombination systems as flexible tools for genome design.

Online content

Any methods, additional references, Nature Portfolio reporting summaries, source data, extended data, supplementary information, acknowledgements, peer review information; details of author contributions and competing interests; and statements of data and code availability are available at <https://doi.org/10.1038/s41586-024-07570-2>.

1. Siguier, P., Gourbeyre, E., Varani, A., Ton-Hoang, B. & Chandler, M. Everyman's guide to bacterial insertion sequences. *Microbiol. Spectr.* **3**, MDNA3-0030-2014 (2015).
2. Durrant, M. G. et al. Bridge RNAs direct modular and programmable recombination of target and donor DNA. *Nature* (in the press).
3. Curcio, M. J. & Derbyshire, K. M. The outs and ins of transposition: from Mu to Kangaroo. *Nat. Rev. Mol. Cell Biol.* **4**, 865–877 (2003).
4. Hickman, A. B. & Dyda, F. Mechanisms of DNA transposition. *Microbiol. Spectr.* **3**, MDNA3-0034-2014 (2015).
5. Perkins-Balding, D., Duval-Valentin, G. & Glasgow, A. C. Excision of IS492 requires flanking target sequences and results in circle formation in *Pseudoalteromonas atlantica*. *J. Bacteriol.* **181**, 4937–4948 (1999).
6. Müller, C., Lauf, U. & Hermann, H. The inverted repeats of IS1384, a newly described insertion sequence from *Pseudomonas putida* strain H, represent the specific target for integration of IS1383. *Mol. Genet. Genomics* **265**, 1004–1010 (2001).
7. Choi, S., Ohta, S. & Ohtsubo, E. A novel IS element, IS621, of the IS110/IS492 family transposes to a specific site in repetitive extragenic palindromic sequences in *Escherichia coli*. *J. Bacteriol.* **185**, 4891–4900 (2003).

8. Partridge, S. R. & Hall, R. M. The IS1111 family members IS4321 and IS5075 have subterminal inverted repeats and target the terminal inverted repeats of Tn21 family transposons. *J. Bacteriol.* **185**, 6371–6384 (2003).
9. Higgins, B. P., Popkowski, A. C., Caruana, P. R. & Karls, A. C. Site-specific insertion of IS492 in *Pseudoalteromonas atlantica*. *J. Bacteriol.* **191**, 6408–6414 (2009).
10. Higgins, B. P., Carpenter, C. D. & Karls, A. C. Chromosomal context directs high-frequency precise excision of IS492 in *Pseudoalteromonas atlantica*. *Proc. Natl Acad. Sci. USA* **104**, 1901–1906 (2007).
11. Rutherford, K. & Van Duyn, G. D. The ins and outs of serine integrase site-specific recombination. *Curr. Opin. Struct. Biol.* **24**, 125–131 (2014).
12. Meinke, G., Bohm, A., Hauber, J., Pisabarro, M. T. & Buchholz, F. Cre recombinase and other tyrosine recombinases. *Chem. Rev.* **116**, 12785–12820 (2016).
13. Smith, M. C. A. et al. Synapsis and DNA cleavage in ϕ C31 integrase-mediated site-specific recombination. *Nucleic Acids Res.* **32**, 2607–2617 (2004).
14. Ariyoshi, M. et al. Atomic structure of the RuvC resolvase: a Holliday junction-specific endonuclease from *E. coli*. *Cell* **78**, 1063–1072 (1994).
15. Yang, W. Nucleases: diversity of structure, function and mechanism. *Q. Rev. Biophys.* **44**, 1–93 (2011).
16. Nishimaru, H. et al. Crystal structure of Cas9 in complex with guide RNA and target DNA. *Cell* **156**, 935–949 (2014).
17. Holm, L. Using Dali for protein structure comparison. *Methods Mol. Biol.* **2112**, 29–42 (2020).
18. Spinola-Amilibia, M., Araújo-Bazán, L., de la Gándara, Á., Berger, J. M. & Arias-Palomo, E. IS21 family transposase cleaved donor complex traps two right-handed superhelical crossings. *Nat. Commun.* **14**, 2335 (2023).
19. Buchner, J. M., Robertson, A. E., Poynter, D. J., Denniston, S. S. & Karls, A. C. Piv site-specific invertase requires a DEDD motif analogous to the catalytic center of the RuvC Holliday junction resolvases. *J. Bacteriol.* **187**, 3431–3437 (2005).
20. Slaymaker, I. M. & Gaudelli, N. M. Engineering Cas9 for human genome editing. *Curr. Opin. Struct. Biol.* **69**, 86–98 (2021).
21. Jinek, M. et al. A programmable dual-RNA-guided DNA endonuclease in adaptive bacterial immunity. *Science* **337**, 816–821 (2012).
22. Zetsche, B. et al. Cpf1 is a single RNA-guided endonuclease of a class 2 CRISPR–Cas system. *Cell* **163**, 759–771 (2015).
23. Altae-Tran, H. et al. The widespread IS200/IS605 transposon family encodes diverse programmable RNA-guided endonucleases. *Science* **374**, 57–65 (2021).
24. Karvelis, T. et al. Transposon-associated TnpB is a programmable RNA-guided DNA endonuclease. *Nature* **599**, 692–696 (2021).
25. Saito, M. et al. Fanzor is a eukaryotic programmable RNA-guided endonuclease. *Nature* **620**, 660–668 (2023).
26. Liu, J. et al. Argonaute2 is the catalytic engine of mammalian RNAi. *Science* **305**, 1437–1441 (2004).
27. Abudayyeh, O. O. et al. C2c2 is a single-component programmable RNA-guided RNA-targeting CRISPR effector. *Science* **353**, aaf5573 (2016).
28. Strecker, J. et al. RNA-guided DNA insertion with CRISPR-associated transposases. *Science* **365**, 48–53 (2019).
29. Klompe, S. E., Vo, P. L. H., Halpin-Healy, T. S. & Sternberg, S. H. Transposon-encoded CRISPR–Cas systems direct RNA-guided DNA integration. *Nature* **571**, 219–225 (2019).
30. Hu, C. et al. Craspase is a CRISPR RNA-guided, RNA-activated protease. *Science* **377**, 1278–1285 (2022).
31. Kato, K. et al. RNA-triggered protein cleavage and cell growth arrest by the type III-E CRISPR nuclease–protease. *Science* **378**, 882–889 (2022).
32. Sternberg, S. H., Redding, S., Jinek, M., Greene, E. C. & Doudna, J. A. DNA interrogation by the CRISPR RNA-guided endonuclease Cas9. *Nature* **507**, 62–67 (2014).
33. Swarts, D. C., van der Oost, J., Jinek, M. Structural basis for guide RNA processing and seed-dependent DNA targeting by CRISPR–Cas12a. *Mol. Cell* **66**, 221–233.e4 (2017).

Publisher's note Springer Nature remains neutral with regard to jurisdictional claims in published maps and institutional affiliations.



Open Access This article is licensed under a Creative Commons Attribution 4.0 International License, which permits use, sharing, adaptation, distribution and reproduction in any medium or format, as long as you give appropriate credit to the original author(s) and the source, provide a link to the Creative Commons licence, and indicate if changes were made. The images or other third party material in this article are included in the article's Creative Commons licence, unless indicated otherwise in a credit line to the material. If material is not included in the article's Creative Commons licence and your intended use is not permitted by statutory regulation or exceeds the permitted use, you will need to obtain permission directly from the copyright holder. To view a copy of this licence, visit <http://creativecommons.org/licenses/by/4.0/>.

© The Author(s) 2024

Methods

Protein and RNA preparation

The IS621 recombinase gene was cloned into a modified pFastBac1 expression vector (Thermo Fisher Scientific), which encodes an N-terminal His₆ tag, a Twin-Strep tag and a human rhinovirus 3C protease cleavage site (Supplementary Table 1). The IS621 protein was expressed in Sf9 cells (Thermo Fisher Scientific), using the Bac-to-Bac baculovirus expression system (Thermo Fisher Scientific). Sf9 cells were cultured in Sf900II medium (Thermo Fisher Scientific), infected with the recombinant baculovirus at a density of approximately 2×10^6 cells per millilitre, and then incubated at 27 °C for 48 h. The cells were collected by centrifugation at 5,000g and stored at -80 °C before use. The Sf9 cells were lysed by sonication in lysis buffer (20 mM Tris-HCl (pH 7.5), 1 M NaCl, 2 mM MgCl₂, 2% Triton X-100 and protease inhibitor cocktail), and the lysate was clarified by centrifugation at 40,000g. The supernatant was mixed with Strep-Tactin XT resin (IBA) at 4 °C for 1 h. The resin was washed with wash buffer (20 mM Tris-HCl (pH 7.5), 500 mM NaCl, 2 mM MgCl₂, 3 mM 2-mercaptoethanol and 10% glycerol), and the protein was eluted with wash buffer containing 80 mM biotin. The eluted protein was purified by size-exclusion chromatography on a Superdex 200 Increase 10/300 GL column (Cytiva), equilibrated with buffer (20 mM Tris-HCl (pH 7.5), 500 mM NaCl, 1 mM dithiothreitol (DTT), 10% glycerol and 2 mM MgCl₂). The peak fractions were collected and stored at -80 °C until use. The S241A and D11A/E60A/D102A/D105A mutants were similarly expressed and purified. The bRNAs were transcribed in vitro with T7 RNA polymerase and purified by 10% denaturing (7 M urea) PAGE (Supplementary Table 1).

Synaptic complex preparation

The IS621-bRNA-dDNA-tDNA synaptic complex was reconstituted by mixing the purified IS621 recombinase, a 177-nt bRNA (177 nt plus 5'-GGG for in vitro transcription), a 44-bp dDNA and a 38-bp tDNA, at a molar ratio of 4:1:1:1. To obtain a synaptic complex with the WT bRNA (pre-strand exchange state), six mismatches were introduced into the top strands of the tDNA and dDNA (Supplementary Table 1). To obtain a synaptic complex with the pre-HSB bRNA (pre-strand exchange locked state) or the post-HSB bRNA (post-strand exchange state), four mismatches were introduced into the top strands of the tDNA and dDNA (Supplementary Table 1). The IS621-bRNA-dDNA-tDNA synaptic complex was purified by size-exclusion chromatography on a Superose 6 Increase 10/300 column (Cytiva), equilibrated with buffer (20 mM Tris-HCl (pH 7.5), 300 mM NaCl, 5 mM MgCl₂ and 1 mM DTT). The peak fraction containing the synaptic complex was concentrated to 0.5–1 mg ml⁻¹, using an Amicon Ultra-4 Centrifugal Filter Unit (MWCO 50 kDa; Millipore). Protein concentrations were measured by the Pierce 660 nm Protein Assay Reagent (Thermo Fisher Scientific).

Cryo-EM analysis

The grids were glow-discharged in low-pressure air at a 10-mA current in a PIB-10 ion generator (Vacuum Device). The synaptic complex solution was applied to a freshly glow-discharged Quantifoil Holey Carbon Grid (R1.2/1.3, Au, 300 mesh) (SPT Labtech) using a Vitrobot Mark IV system (Thermo Fisher Scientific) at 4 °C, with a waiting time of 10 s and a blotting time of 6 s under 100% humidity conditions. The grids were plunge-frozen in liquid ethane cooled at liquid nitrogen temperature.

The grids containing the synaptic complex with the WT bRNA or the pre-HSB bRNA were transferred to a Titan Krios G3i electron microscope (Thermo Fisher Scientific) running at 300 kV and equipped with a Gatan Quantum-LS Energy Filter (GIF) and a Gatan K3 Summit direct electron detector. The grid containing the synaptic complex with the post-HSB bRNA was transferred to a Titan Krios G4 electron microscope (Thermo Fisher Scientific) running at 300 kV and equipped with a Gatan Quantum-LS Energy Filter and a Gatan K3 Summit direct electron detector. Imaging was performed at a nominal magnification of $\times 105,000$,

corresponding to a calibrated pixel size of 0.83 Å per pixel. For the synaptic complex with the WT bRNA, each movie was dose fractionated to 50 frames and recorded using the correlated double-sampling mode at a dose rate of $7.7 \text{ e}^- \text{ px}^{-1} \text{ s}^{-1}$, resulting in a total accumulated exposure of $50 \text{ e}^- \text{ Å}^{-2}$ of the specimen. For the synaptic complex with the pre-HSB bRNA, each movie was dose fractionated to 48 frames and recorded using the normal mode at a dose rate of $14.7 \text{ e}^- \text{ px}^{-1} \text{ s}^{-1}$, resulting in a total accumulated exposure of $49 \text{ e}^- \text{ Å}^{-2}$ of the specimen. For the synaptic complex with the post-HSB bRNA, each movie was dose fractionated to 64 frames and recorded using the correlated double-sampling mode at a dose rate of $9.5 \text{ e}^- \text{ px}^{-1} \text{ s}^{-1}$, resulting in a total accumulated exposure of $62 \text{ e}^- \text{ Å}^{-2}$ of the specimen. The data were automatically acquired using the image-shift method in the EPU software (Thermo Fisher Scientific), with a defocus range of -0.8 to -2.0 μm.

The data were processed using the cryoSPARC v4.3.0 software package³⁴. The dose-fractionated movies were aligned using Patch motion correction, and the contrast transfer function (CTF) parameters were estimated using patch-based CTF estimation. For the synaptic complex with the WT bRNA, particles were automatically picked using Blob picker and template picker, followed by reference-free 2D classification to curate particle sets. The particles were further curated by heterogeneous refinement, using the map derived from cryoSPARC ab initio reconstruction as the template. The best-class particle set was refined using non-uniform refinement, yielding a map at 2.58 Å resolution. Local motion correction followed by non-uniform refinement with CTF value optimization yielded a map at 2.52 Å resolution, according to the Fourier shell correlation (FSC) = 0.143 criterion³⁵. The local resolution was estimated by BlocRes in cryoSPARC.

For the synaptic complex with the pre-HSB bRNA, particles were automatically picked using template picker, followed by reference-free 2D classification of the WT bRNA sets. The particles were further curated by heterogeneous refinement, using the WT bRNA maps as a template. The best-class particle set was refined using homogeneous refinement and non-uniform refinement, yielding a map at 2.79 Å resolution. Local motion correction followed by non-uniform refinement with CTF value optimization yielded a map at 2.72 Å resolution, according to the FSC = 0.143 criterion. The local resolution was estimated by BlocRes in cryoSPARC.

For the synaptic complex with the post-HSB bRNA, particles were automatically picked using template picker, followed by reference-free 2D classification of the WT bRNA datasets. The particles were further curated by heterogeneous refinement, using the WT bRNA maps as a template. To further distinguish the conformational heterogeneity, the selected particles after homogeneous refinement were divided into four classes using 3D classification. The particle sets in the two selected classes were further refined using homogeneous refinement and heterogeneous refinement. Non-uniform refinement with CTF value optimization yielded maps at 2.88 Å resolution (state 1) and 2.73 Å resolution (state 2), according to the FSC = 0.143 criterion. The local resolution was estimated by BlocRes in cryoSPARC.

Model building and validation

The models of the IS621-bRNA-dDNA-tDNA synaptic complexes were manually built using COOT³⁶, starting from a model predicted by ColabFold³⁷. The models were refined using phenix.real_space_refine³⁸ and Servalcat³⁹ against unsharpened half maps. The models were validated using MolProbity⁴⁰. The statistics of the 3D reconstruction and model refinement are summarized in Extended Data Table 1. The molecular graphics and cryo-EM density map figures were prepared with CueMol (<http://www.cuemol.org>) or UCSF ChimeraX⁴¹.

In vitro recombination assays

For in vitro recombination assays, linear tDNA and dDNA substrates were synthesized by Eurofins Genomics, and labelled with FAM or Cy5 at the 5' end of the top or bottom strand (Supplementary Table 1).

Article

The tDNA (0.1 μM) and dDNA (0.1 μM) substrates were mixed with the pre-incubated IS621–bRNA complex (1.4 μM) in 100 μl buffer (20 mM Tris-HCl (pH 7.5), 300 mM NaCl, 5 mM MgCl₂ and 1 mM DTT), and then the reactions were incubated at 37 °C for 1 h. The reaction mixture was mixed with proteinase K (Nacalai Tesque) and then boiled at 95 °C for 3 min in denaturing buffer (7 M urea). The samples were analysed by 18% urea-PAGE, and fluorescent signals were imaged using FUSION Solo S (Vilber Bio Imaging). For gel source data, see Supplementary Fig. 7.

Microscale thermophoresis

Microscale thermophoresis experiments were performed using a Monolith NT.115pico Series instrument (NanoTemper), as previously described². The IS621 recombinase was labelled using the RED-MALEIMIDE 2nd generation cysteine reactive kit (NanoTemper). The labelled protein was eluted in buffer (20 mM Tris-HCl (pH 7.5), 500 mM NaCl, 5 mM MgCl₂, 1 mM DTT and 0.01% Tween 20). To determine the affinity of the IS621 recombinase for RNA, 20 nM recombinase was incubated with a dilution series (0.076–250 nM) of the bRNA (177 nt), its reverse complement (177 nt) or the bRNA mutant lacking the 5' stem loop (146 nt). Microscale thermophoresis experiments were performed at 37 °C using premium capillaries (NanoTemper) at medium microscale thermophoresis power with the LED excitation power set to automatic (excitation ranged from 10% to 50%). Data were analysed using the NanoTemper MO.affinity analysis software package, and raw data were plotted using GraphPad Prism 9 (GraphPad).

Bacterial recombination assays

Bacterial recombination assays were performed, as previously described². In brief, *E. coli* BL21(DE3) cells (NEB) were co-transformed with a pTarget plasmid encoding a target sequence and a T7-inducible IS621 recombinase, and a pDonor plasmid encoding a bRNA, a donor sequence and GFP, such that, upon recombination into pRecombinant, GFP expression would be activated by the synthetic Bba_R0040 promoter adjacent to the target site (Supplementary Table 1). pDonor encodes the WT IS621 donor sequences and pTarget encodes a DNA sequence not found in the *E. coli* genome, and the bRNA was programmed to recombine these two DNA sequences. Co-transformed cells were plated on fresh LB agar containing kanamycin, chloramphenicol and 0.07 mM IPTG to induce recombinase expression. Plates were incubated at 37 °C for 16 h and then at room temperature for 8 h. Hundreds of colonies were scraped from the plate, resuspended in terrific broth and diluted to an appropriate concentration for flow cytometry. About 5×10^4 cells were analysed on a NovoCyte Quanteon Flow Cytometer to assess the fluorescence intensity of GFP-expressing cells (Supplementary Fig. 8). The mean fluorescence intensity of the population (including both GFP⁺ and GFP⁻ cells) was plotted.

Covariation analysis

Covariation analysis to identify base-pairing potential between bRNA and tDNA or dDNA was performed, as previously described². In brief, IS621 orthologue sequences were searched (blastp) against a curated database of IS110 elements extracted from publicly available genomic sequence archives⁴². Next, a covariance model (CM) of the bRNA primary and secondary structures was used to identify homologues of the bRNA sequence in the non-coding ends of these orthologue sequences⁴³. Target and donor sequences centred around the predicted core were extracted. Predicted bRNA sequences were aligned using the cmalign tool in the Infernal package. Two paired alignments were then generated that contained concatenated target and bRNA sequences, and concatenated donor and bRNA sequences. These alignments were analysed using CCMpred ('-n 100') to identify covarying nucleotides between target–donor and bRNA sequences⁴⁴. These covariation scores were normalized and multiplied by the sign of a base-pairing concordance score to produce the covariation score scale, which ranged from –1 (top strand base pairing) to +1 (bottom strand base pairing).

Reporting summary

Further information on research design is available in the Nature Portfolio Reporting Summary linked to this article.

Data availability

Cryo-EM density maps have been deposited in the Electron Microscopy Data Bank under the accession codes EMD-37827 (pre-strand exchange state), EMD-37828 (pre-strand exchange locked state), EMD-37829 (Holliday junction intermediate state) and EMD-37830 (Holliday junction resolution state). Atomic coordinates have been deposited in the Protein Data Bank under IDs 8WT6 (pre-strand exchange state), 8WT7 (pre-strand exchange locked state), 8WT8 (Holliday junction intermediate state) and 8WT9 (Holliday junction resolution state). The raw images have been deposited in the Electron Microscopy Public Image Archive, under the accession code EMPIAR-11804.

- Punjani, A., Rubinstein, J. L., Fleet, D. J. & Brubaker, M. A. cryoSPARC: algorithms for rapid unsupervised cryo-EM structure determination. *Nat. Methods* **14**, 290–296 (2017).
- Rosenthal, P. B. & Henderson, R. Optimal determination of particle orientation, absolute hand, and contrast loss in single-particle electron cryomicroscopy. *J. Mol. Biol.* **333**, 721–745 (2003).
- Emsley, P., Lohkamp, B., Scott, W. G. & Cowtan, K. Features and development of Coot. *Acta Crystallogr. D Biol. Crystallogr.* **66**, 486–501 (2010).
- Jumper, J. et al. Highly accurate protein structure prediction with AlphaFold. *Nature* **596**, 583–589 (2021).
- Afonine, P. V. et al. Real-space refinement in PHENIX for cryo-EM and crystallography. *Acta Crystallogr. D Struct. Biol.* **74**, 531–544 (2018).
- Yamashita, K., Palmer, C. M., Burnley, T. & Murshudov, G. N. Cryo-EM single-particle structure refinement and map calculation using Servalcat. *Acta Crystallogr. D Struct. Biol.* **77**, 1282–1291 (2021).
- Williams, C. J. et al. MolProbity: more and better reference data for improved all-atom structure validation. *Protein Sci.* **27**, 293–315 (2018).
- Pettersen, E. F. et al. UCSF ChimeraX: structure visualization for researchers, educators, and developers. *Protein Sci.* **30**, 70–82 (2021).
- Sayers, E. W. et al. Database resources of the National Center for Biotechnology Information. *Nucleic Acids Res.* **50**, D20–D26 (2022).
- Nawrocki, E. P. & Eddy, S. R. Infernal 1.1: 100-fold faster RNA homology searches. *Bioinformatics* **29**, 2933–2935 (2013).
- Ekeberg, M., Lökvist, C., Lan, Y., Weigt, M. & Aurell, E. Improved contact prediction in proteins: using pseudolikelihoods to infer Potts models. *Phys. Rev. E Stat. Nonlin. Soft Matter Phys.* **87**, 012707 (2013).

Acknowledgements We thank K. Kato for assistance with the structural determination, and the staff scientists at The University of Tokyo's cryo-EM facility, especially Y. Sakamaki, for help with cryo-EM data collection. M.H. is supported by JSPS KAKENHI grant number 23K14133, Takeda Medical Research Foundation and JST, ACT-X grant number JPMJAX232F. N.T.P. was partially supported by the NIH Biology and Biotechnology of Cell and Gene Therapy Training Program (T32GM139780). M.G.D., J.S.A. and S.K. are supported by funding from the Arc Institute. P.D.H. is supported by funding from the Arc Institute, Rainwater Foundation, Curci Foundation, Rose Hill Innovators Program, S. Altman, V. and N. Khosla and anonymous gifts to the Hsu laboratory. H.N. is supported by JSPS KAKENHI grant numbers 21H05281 and 22H00403, Takeda Medical Research Foundation, the Inamori Research Institute for Science and JST, CREST grant number JPMJCR23B6.

Author contributions M.H. and S.O. performed sample preparation, with assistance from T.S. and Y.I. M.H. performed the biochemical experiments and cryo-EM data collection with assistance from S.O. and N.N. M.H. performed the cryo-EM image processing. M.H., K.Y. and H.N. performed the model building. M.H. and S.O. performed the in vitro recombination assays. N.T.P. and J.J.P. performed the bacterial recombination assays. M.G.D. performed the computational analysis. J.S.A. performed the binding experiments. M.H. and H.N. wrote the manuscript with assistance from N.T.P., M.G.D., A.P., S.K., K.Y. and P.D.H. S.K., P.D.H. and H.N. supervised the research.

Competing interests P.D.H. acknowledges outside interests in Stylus Medicine, Spotlight Therapeutics, Circle Labs, Arbor Biosciences, Varda Space, Vial Health, Serotiny and LabSimply, where he holds various roles as co-founder, director, scientific advisory board member or consultant. M.G.D. acknowledges outside interest in Stylus Medicine. M.H., N.T.P., M.G.D., J.S.A., S.K., P.D.H. and H.N. are listed as co-inventors on patent applications related to the structure-based engineering of IS110 systems, filed by Arc Institute, The University of Tokyo and the University of California. All other authors declare no competing interests.

Additional information

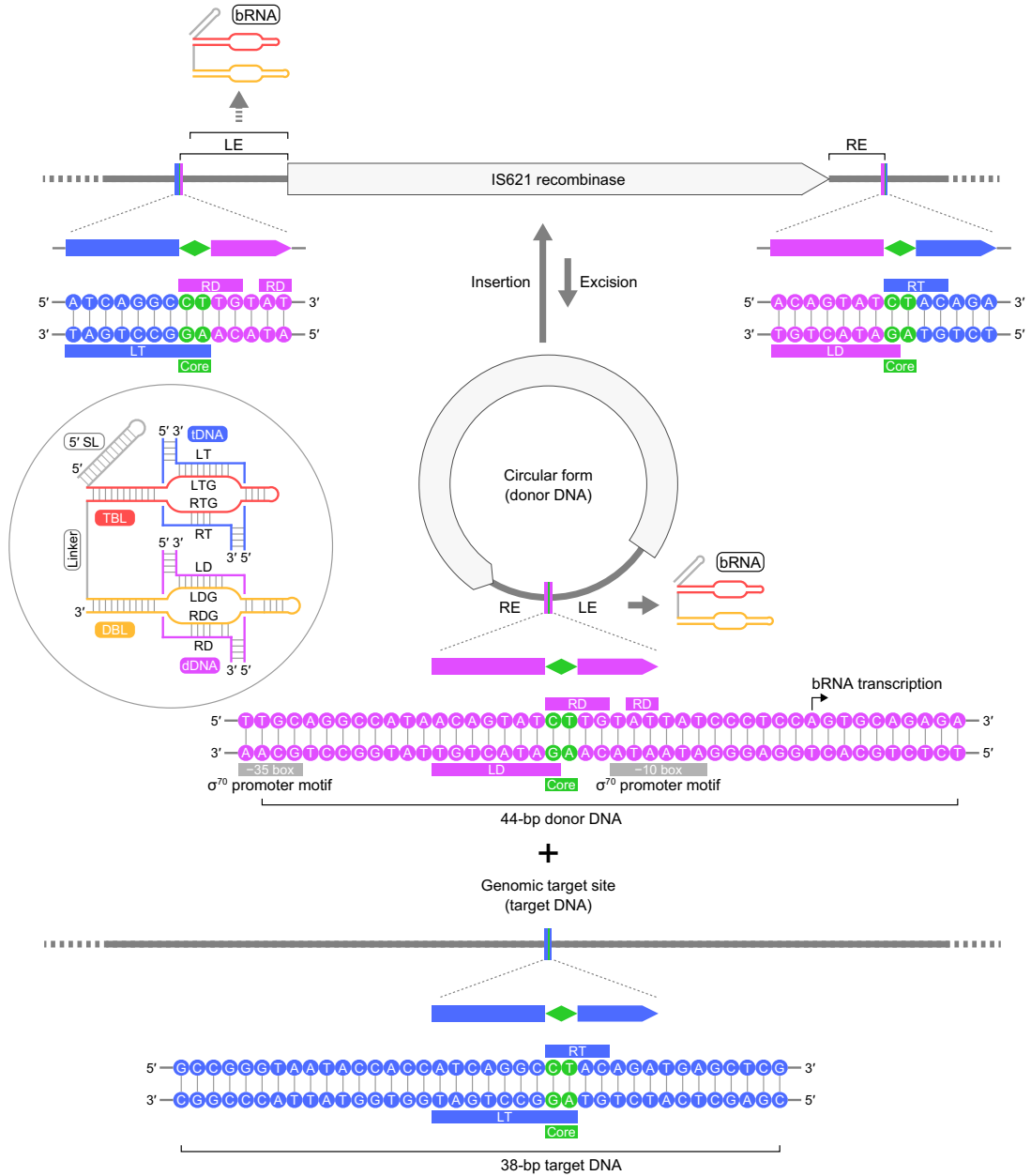
Supplementary information The online version contains supplementary material available at <https://doi.org/10.1038/s41586-024-07570-2>.

Correspondence and requests for materials should be addressed to Patrick D. Hsu or Hiroshi Nishimasa.

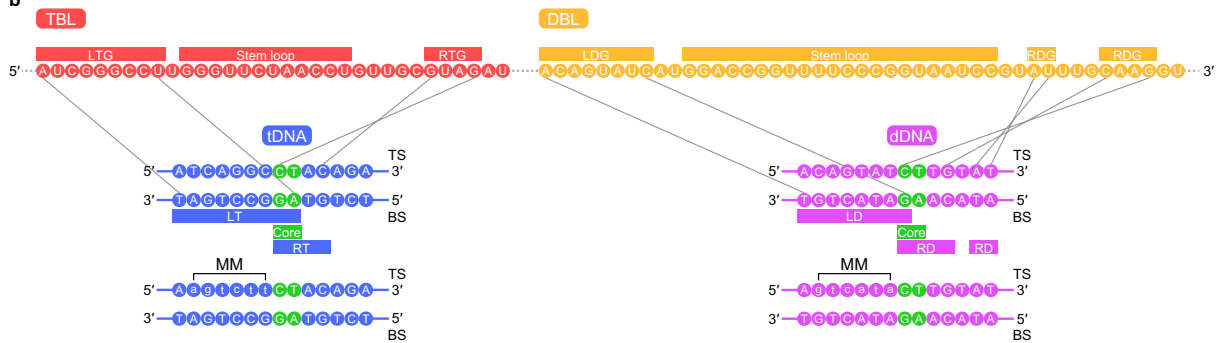
Peer review information Nature thanks the anonymous reviewers for their contribution to the peer review of this work.

Reprints and permissions information is available at <http://www.nature.com/reprints>.

a



b

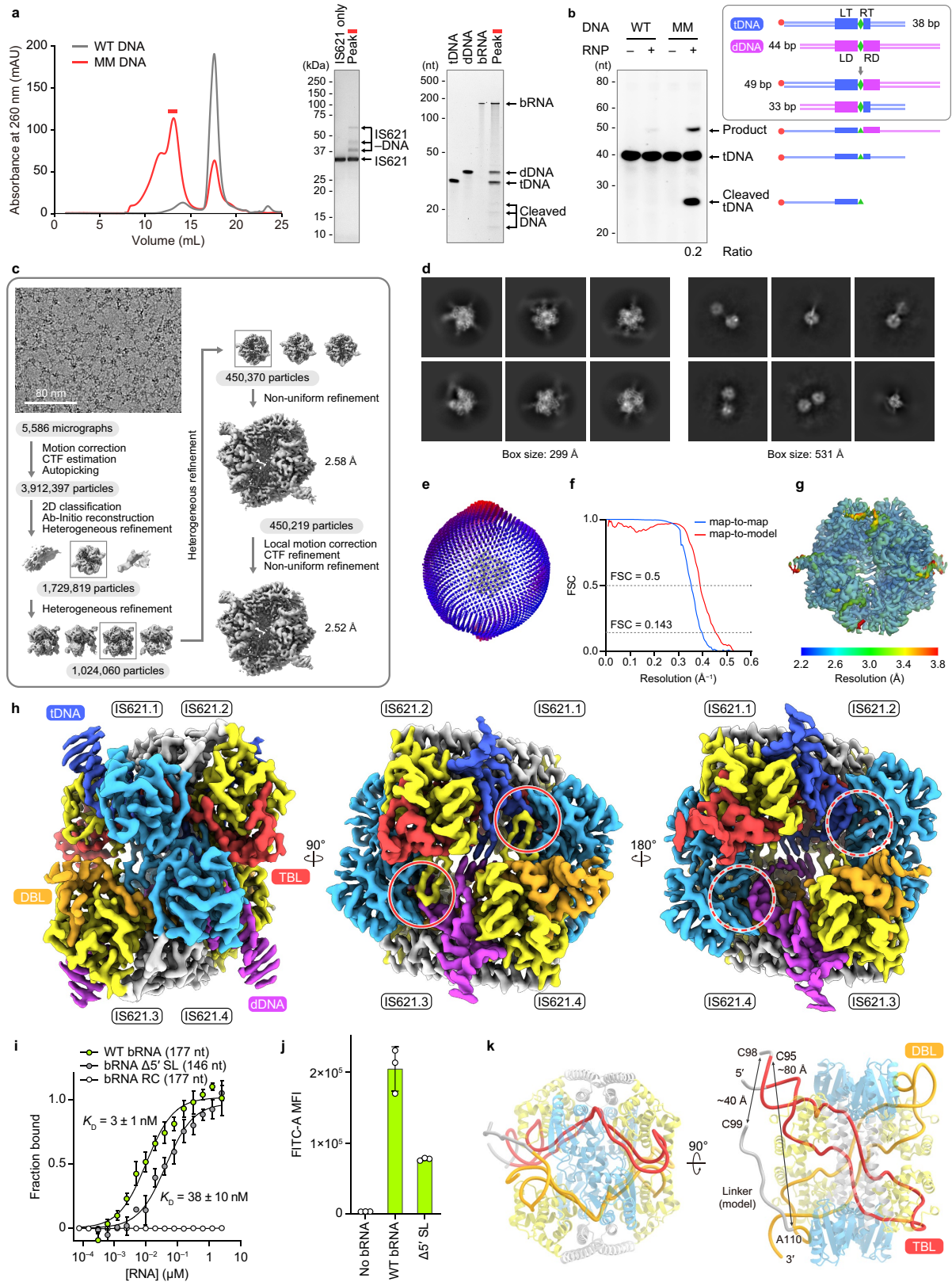


Extended Data Fig. 1 | See next page for caption.

Article

Extended Data Fig. 1 | IS621 insertion sequence element. (a) Transposition cycle of the IS621 insertion sequence element. The IS621 elements consist of the left end (LE), the recombinase-coding sequence, and the right end (RE), flanked by the CT core dinucleotide sequences at both ends. The transposition cycle of the IS621 elements consists of excision (generation of a circular form) and insertion (recombination between the circular form and genomic target sites) steps. In the excision step, recombination would occur between the 5' left target (LT)-core-right donor (RD) region and the 3' left donor (LD)-core-right target (RT) region in the IS621 locus, resulting in the LT-core-RT region in the original genomic site and the LD-core-RD region at the RE-LE junction in the circular form. Importantly, the RE-LE junction contains the reconstituted σ^{70} -like promoter sequence, since RE and LE contain a -35 box and a -10 box, respectively². Thus, the bRNA encoded in the LE is expressed downstream of

the core sequence at the RE-LE junction in the circular intermediate². However, it remains unclear whether the excision is mediated by the IS621-bRNA complex and, if so, how the IS621-bRNA complex accomplishes both excision and insertion reactions. For our cryo-EM analysis, we used the 44-bp donor DNA (the RE-LE junction with the LD-core-RD sequence in the circular form) and the 38-bp target DNA (the genomic target site with the LT-core-RT sequence) from the natural IS621 element found in *E. coli*, with the indicated minor modifications to assist structural analysis. 5' SL, 5' stem loop; TBL, target-binding loop; DBL, donor-binding loop; LTG, left target guide; RTG, right target guide; LDG, left donor guide; RDG, right donor guide; TS, top strand; BS, bottom strand. **(b)** Schematics showing base-pairing between the bRNA and tDNA/dDNA. Mismatched (MM) nucleotides introduced to the top strands for the structural analysis are shown as lower-case letters.



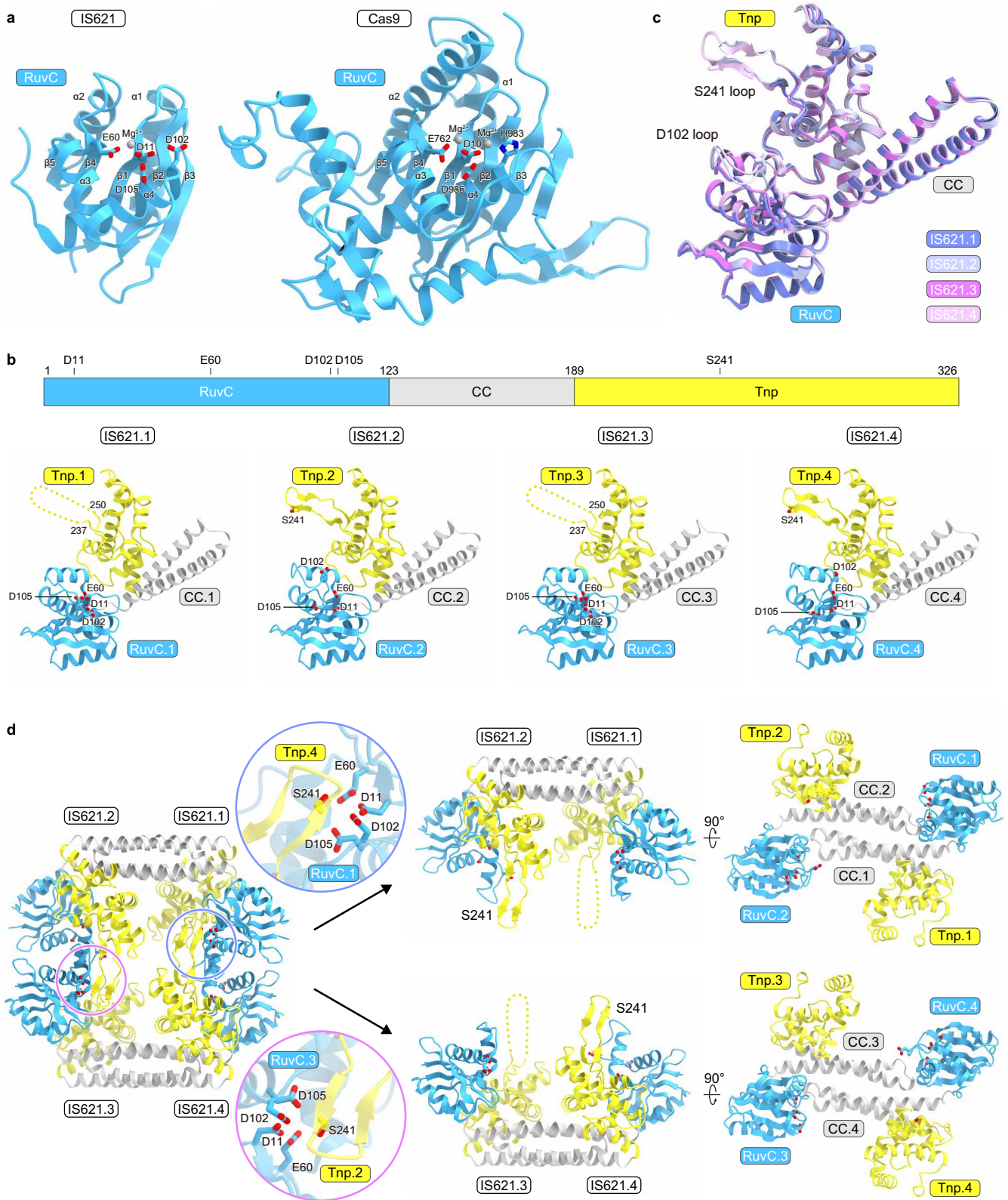
Extended Data Fig. 2 | See next page for caption.

Article

Extended Data Fig. 2 | Cryo-EM analysis of the IS621 synaptic complex.

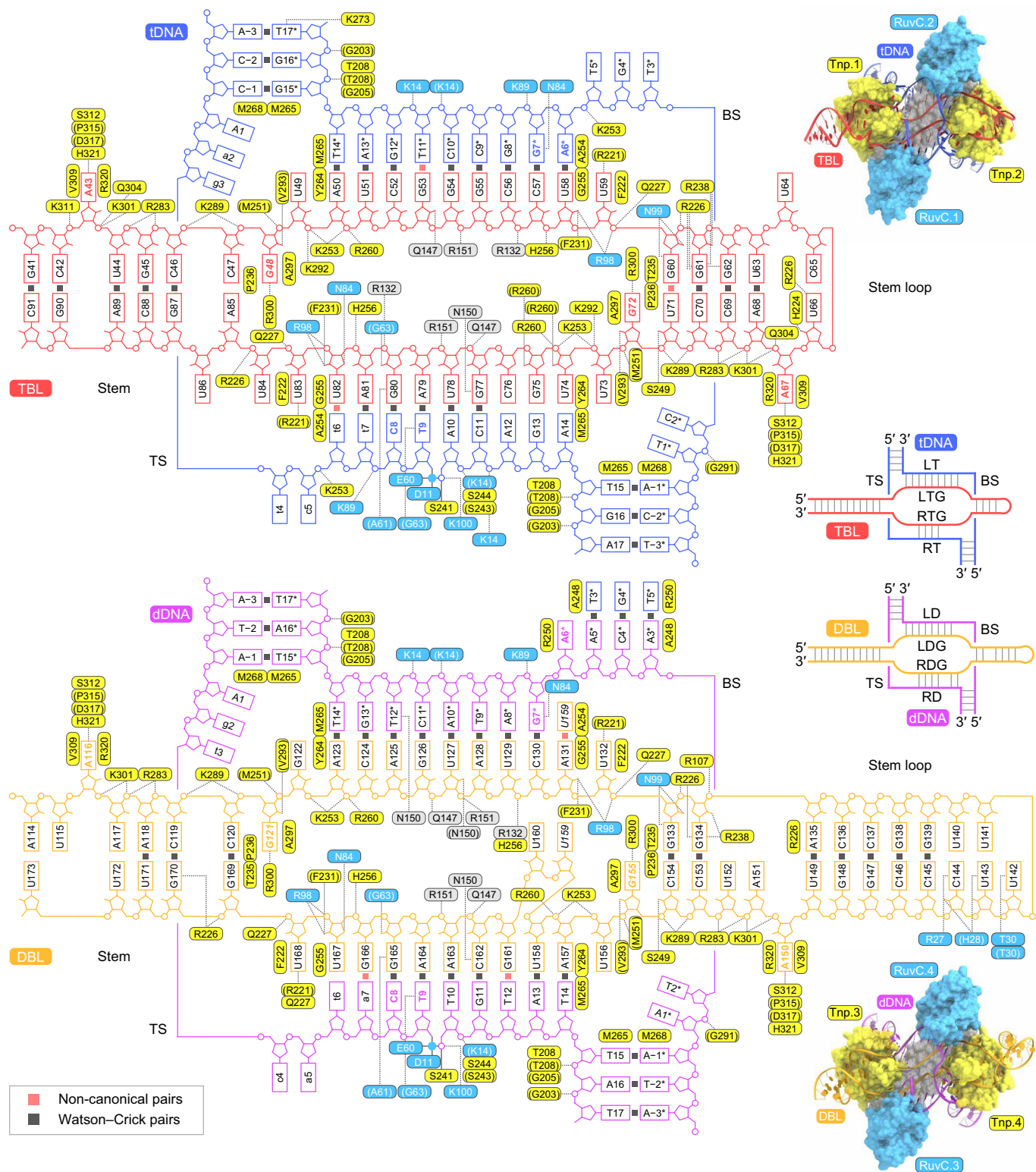
(a) Preparation of the IS621–bRNA–dDNA–tDNA synaptic complex. The IS621 recombinase, bRNA, and dDNA/tDNA (containing no mismatch (WT) or 6-nt mismatches (MM) at positions 2–7 in dDNA and tDNA) were mixed, and then purified by a Superose 6 Increase 10/300 column. The peak fraction of the synaptic complex with the mismatched DNA (indicated by a red line) was analyzed by SDS-PAGE (10–20%) and TBE–urea PAGE (15%). The proteins and nucleic acids were visualized with CBB and SYBR Gold, respectively. We observed three slower-migrating bands that may correspond to covalent IS621–DNA intermediates during recombination (probably IS621–dDNA, IS621–tDNA, and IS621–dDNA–tDNA). Experiments were repeated at least three times with similar results. **(b)** In vitro DNA recombination experiments. The 38-bp tDNA and 44-bp dDNA substrates (containing no mismatch (WT) or 6-nt mismatches (MM) at positions 2–7 in their top strands) were incubated with the IS621–bRNA complex at 37 °C for 1 h, and then the reaction was analyzed using an 18% TBE–urea gel. The tDNA was labeled with Cy5 at the 5' end of the top strand. The band intensities of the product and cleaved DNAs were quantified, and the recombination ratios (product DNA / product DNA + cleaved DNA) were calculated. Experiments were repeated at least three times with similar results. **(c)** Single-particle cryo-EM image processing workflow. **(d)** Representative 2D

averaged class images. **(e)** Angular distribution of particles in the final reconstruction. **(f)** Fourier shell correlation (FSC) curves. The map-to-map FSC curve was calculated between the two independently refined half-maps after masking (blue line), and the overall resolution was determined by the gold standard FSC = 0.143 criterion. The map-to-model FSC curve was calculated between the refined atomic model and the full map (red line). **(g, h)** Cryo-EM density maps, colored according to the local resolution **(g)** and the protein domains **(h)**. In **(h)**, the active sites with the ordered and disordered S241 residues are indicated by red solid and dashed circles, respectively. **(i)** Effects of 5' SL deletion on bRNA binding to the IS621 recombinase. Binding of the purified IS621 recombinase to the bRNA, its reverse complement (RC), or the bRNA lacking the 5' SL (nucleotides A1–U33) (Δ 5' SL) was analyzed using microscale thermophoresis. Data are shown as mean \pm SEM for three technical replicates. **(j)** Effects of 5' SL deletion on IS621-mediated recombination in *E. coli*. Data are shown as mean \pm SD for three biological replicates. **(k)** Distance between TBL and DBL. Nucleotides U96–A109 are disordered in the present structure. Modeling of nucleotides U96–A109 (colored grey) suggests that C98 and C99 are ~40-Å apart, indicating that the TBL and DBL in the synaptic complex structure are derived from two different bRNA molecules.



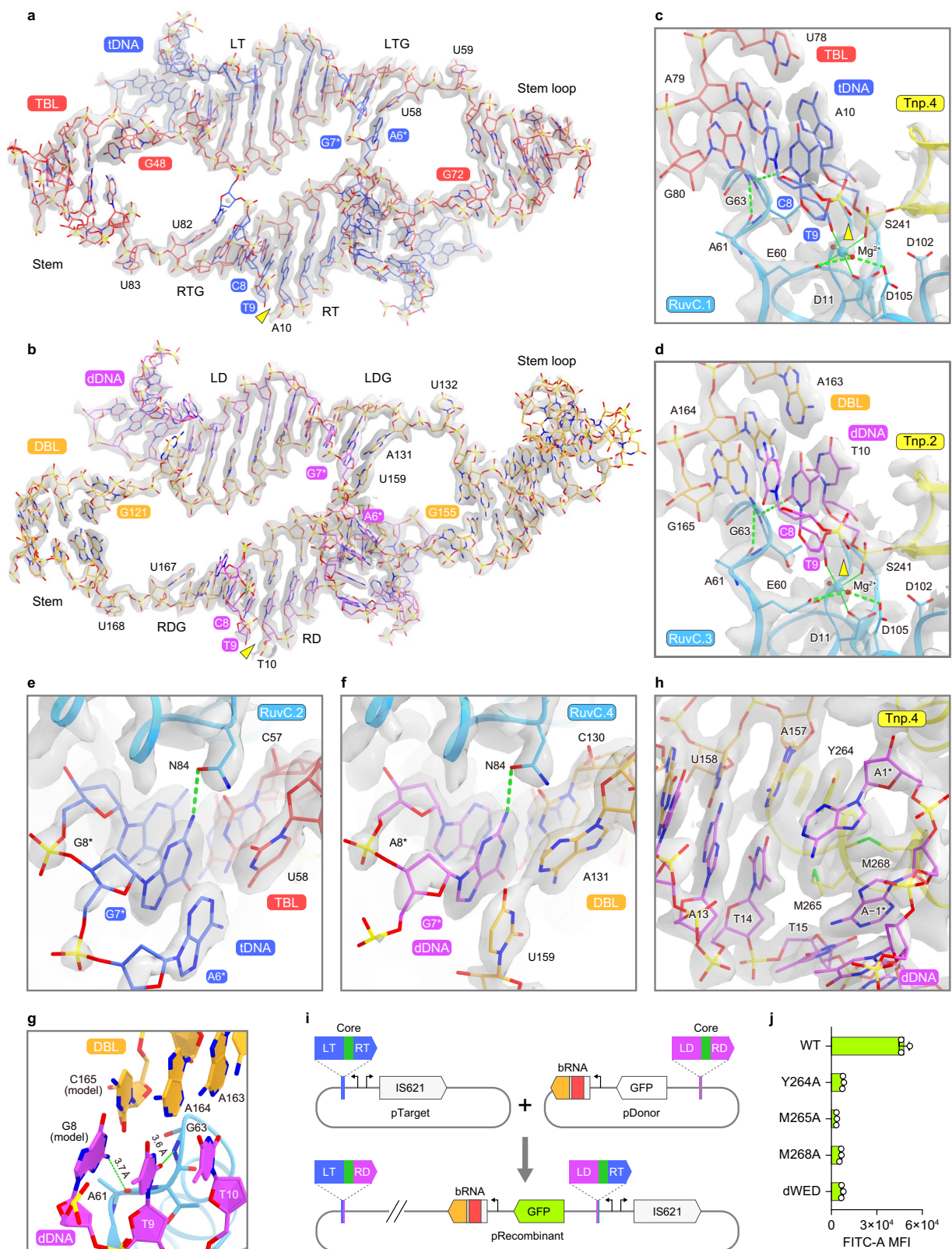
Extended Data Fig. 3 | IS621 recombinase structure. (a) Structural comparison of the RuvC domains of IS621 and Cas9 (PDB: 7S4X). The catalytic residues are shown as stick models. The core α -helices and β -strands are labeled. The RuvC active site of IS621 plays a role in coordinating a Mg^{2+} ion that stabilizes the 5'-phosphoserine DNA intermediates, thereby facilitating DNA cleavage and religation. In contrast, most RuvC domains, such as that of Cas9, bind two Mg^{2+} ions and catalyse the DNA cleavage reaction (*i.e.*, the nucleophilic attack of an

activated water molecule on the scissile phosphodiester bond in a substrate DNA). (b) Structures of the four IS621 protomers. The disordered S241 loops in IS621.1 and IS621.3 are indicated by dotted lines. (c) Superimposition of the RuvC domains in the four IS621 protomers. (d) Structure of the IS621 tetramer. The active sites formed by RuvC.1-Tnp.4 and RuvC.3-Tnp.2 are indicated by blue and magenta circles, respectively.



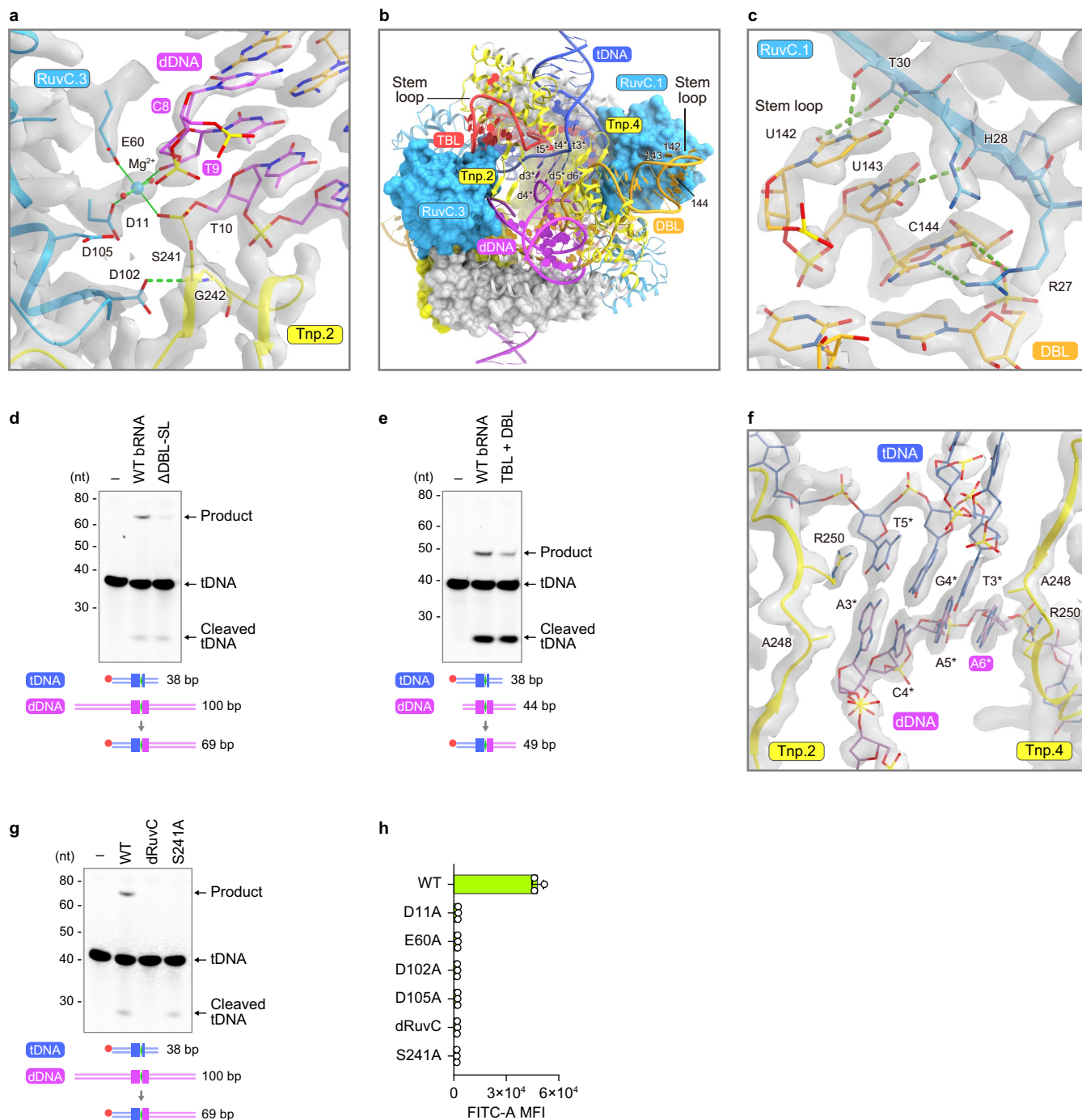
Extended Data Fig. 4 | Schematic of interactions between IS621 and nucleic acids. A43/A67/A116/A150 and G48/G72/G121/G155, common structural features in the TBL and DBL, and the core nucleotides (tC8/tT9/tA6*/tG7* and dC8/dT9/dA6*/dG7*) are highlighted in bold. G48/G72/G121/G155 and U159, which adopt

the *syn* conformation, are shown in italics. The Mg²⁺ ions are depicted as cyan circles. Non-canonical base-pairs are indicated by red squares. The IS621 residues that interact with the nucleic acids through their main chains are shown in parentheses.



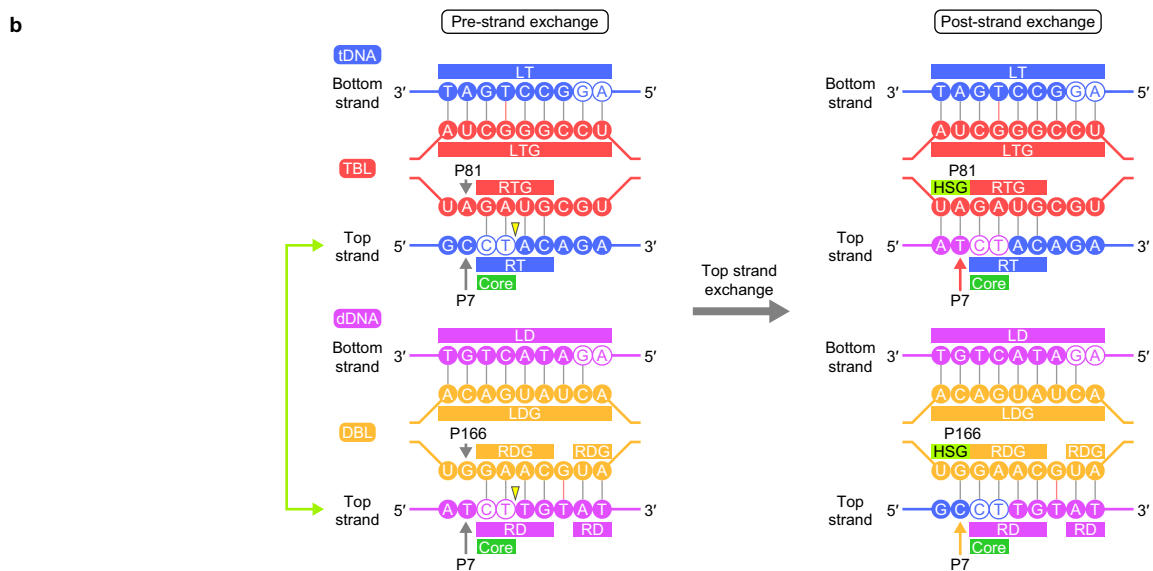
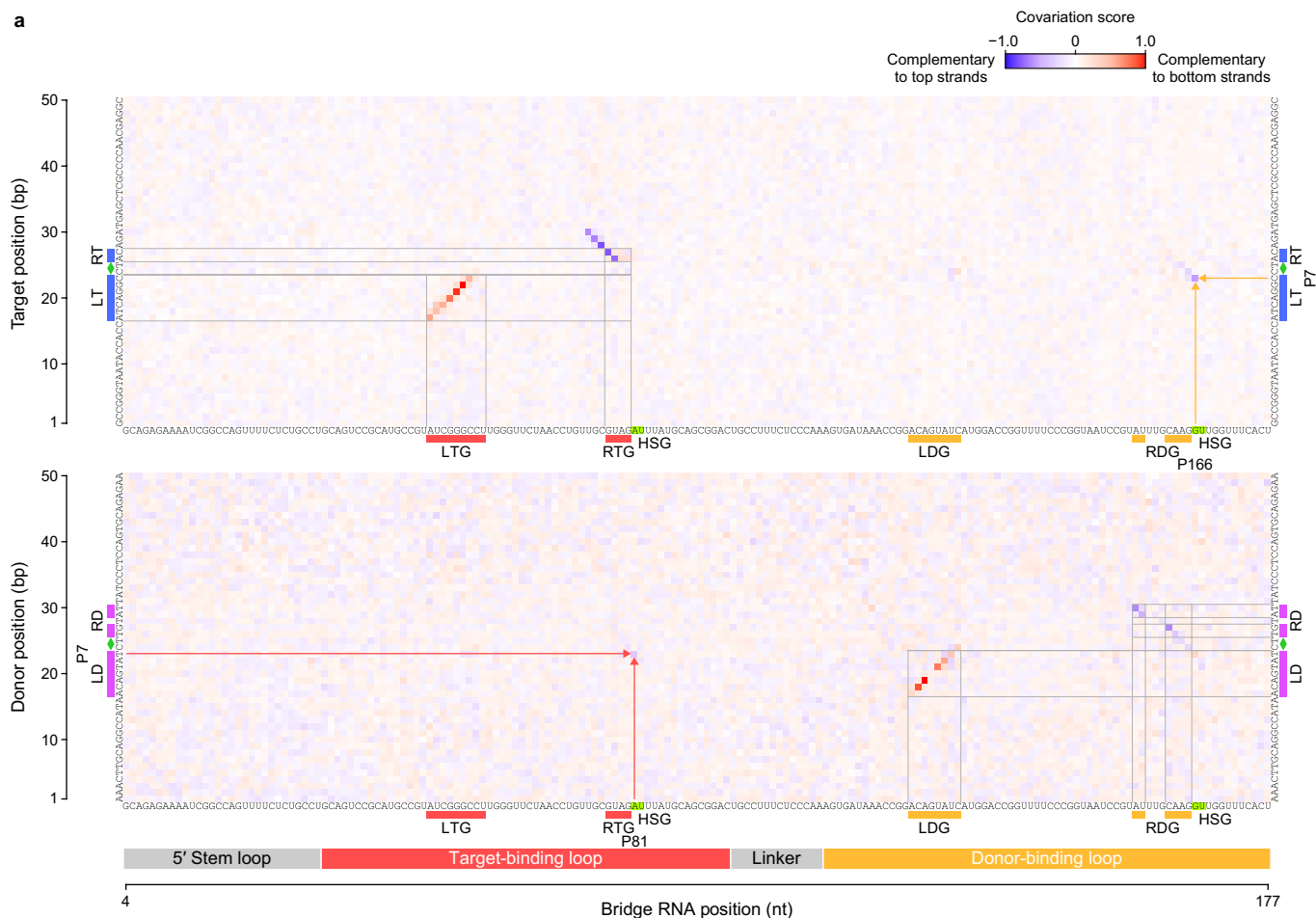
Extended Data Fig. 5 | DNA recognition mechanism. (a, b) Structures of TBL-tDNA (a) and DBL-dDNA (b). (c, d) Recognition of the CT core sequences in tDNA (c) and dDNA (d). (e, f) Recognition of the CT core-complementary sequences in tDNA (e) and dDNA (f). (g) Modeling of dG8 into the dDNA as part of the core dinucleotide. (h) Interaction between the DNA and the hydrophobic wedge. Similar interactions are observed in the four protomers. In (a-f) and (h), cryo-EM density maps are shown as grey semi-transparent surfaces. (i) Schematic

of the bacterial recombination assays. Successful recombination between pTarget and pDonor places the gene encoding green fluorescent protein (GFP) downstream of the synthetic promoter, resulting in fluorescence. IS621, the IS621 recombinase. (j) DNA recombination activities of the WT IS621 and the hydrophobic-wedge mutants in the bacterial recombination assays. Data are shown as mean \pm SD for three biological replicates. dWED, Y264A/M265A/M268A.



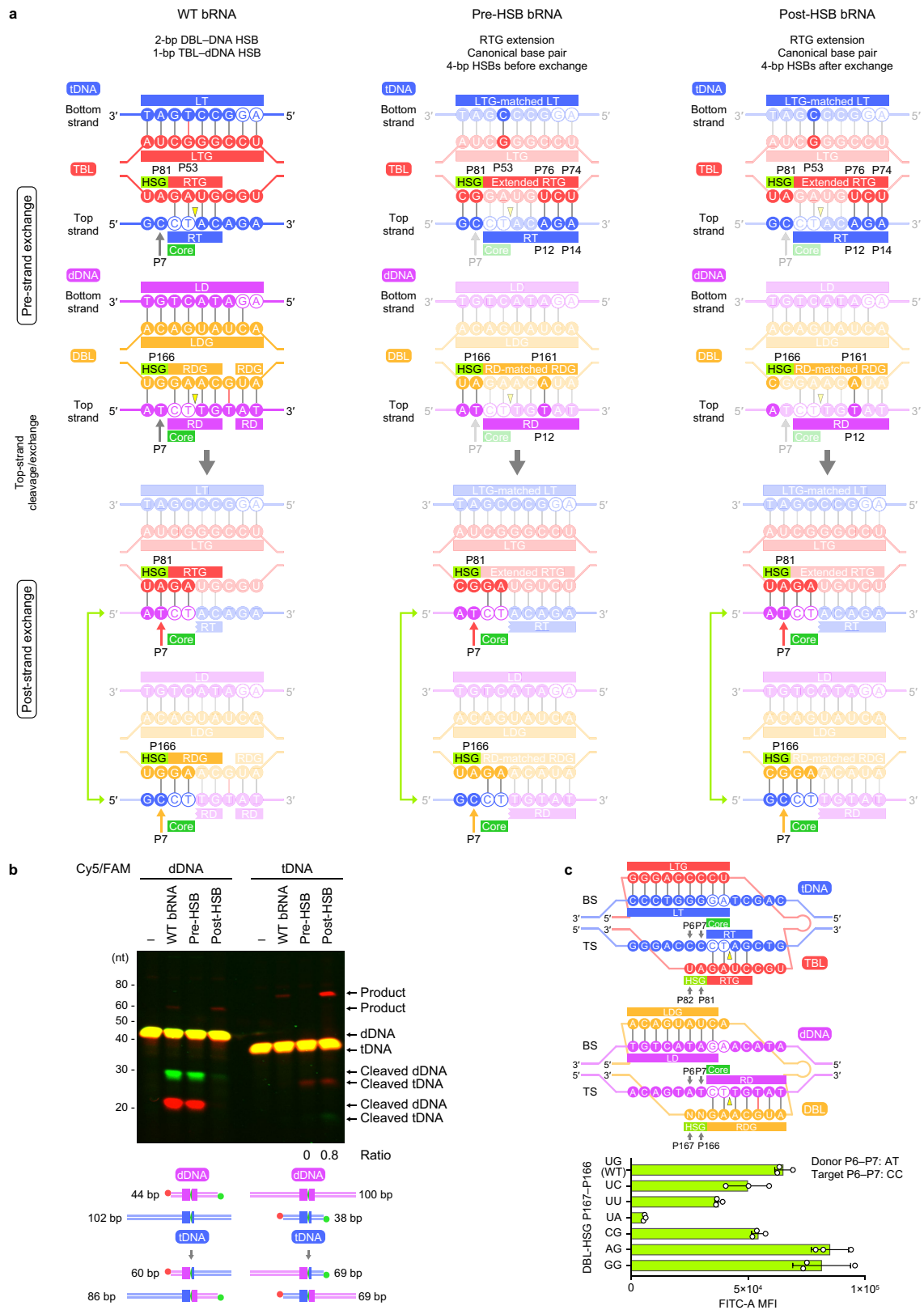
Extended Data Fig. 6 | Synaptic complex formation. (a) Interactions between RuvC.3 and Tnp.2. Similar interactions are observed between RuvC.1 and Tnp.4. (b) Interface between the IS621-TBL-tDNA and IS621-DBL-dDNA dimeric complexes. Nucleotides T3*-T5* in the target DNA and nucleotides dA3*-dA6* in the donor DNA are labeled as t3*-t5* and d3*-d6*, respectively. (c) Interactions between RuvC.1 and DBL-SL. (d) In vitro DNA recombination activities of IS621 in complex with the WT bRNA or the ΔDBL-SL bRNA mutant, in which nucleotides C137-G147 were replaced with GAAA. The tDNA (38 bp) substrate was labeled with Cy5 at the 5' end of the top strand. The Cy5-tDNA (38 bp) and non-labeled dDNA (100 bp) were incubated with the IS621-bRNA complex at 37 °C for 1 h, and then the reaction was analyzed using an 18% TBE-urea gel. Recombination between the Cy5-tDNA and dDNA yields a 69-bp Cy5-labeled product. Experiments were repeated at least three times with similar results. (e) In vitro DNA recombination activities of IS621 in complex with the WT bRNA or separated TBL (nucleotides 31-104) and DBL (nucleotides 99-177). The tDNA (38 bp) substrate was labeled with Cy5 at the 5' end of the top strand. The Cy5-tDNA (38 bp) and non-labeled dDNA (44 bp) (containing 6-nt mismatches

in their top strands) were incubated with the IS621-bRNA complex at 37 °C for 1 h, and then the reaction was analyzed using an 18% TBE-urea gel. Recombination between the Cy5-tDNA and dDNA yields a 49-bp Cy5-labeled product. Experiments were repeated at least three times with similar results. (f) Base-pairing between tDNA and dDNA. In (a), (c), and (f), cryo-EM density maps are shown as grey semi-transparent surfaces. (g) DNA recombination activities of the WT IS621 and the active-site mutants in the in vitro recombination assays. The tDNA (38 bp) substrate was labeled with Cy5 at the 5' end of the top strand. The Cy5-tDNA (38 bp) and non-labeled dDNA (100 bp) were incubated with the IS621-bRNA complex at 37 °C for 1 h, and then the reaction was analyzed using an 18% TBE-urea gel. Recombination between the Cy5-tDNA and dDNA yields a 69-bp Cy5-labeled product. Experiments were repeated at least three times with similar results. dRuvC, D11A/E60A/D102A/D105A. (h) DNA recombination activities of the WT IS621 and the active-site mutants in the bacterial recombination assays. Data are shown as mean ± SD for three biological replicates.



Extended Data Fig. 7 | Covariation analysis. (a) Nucleotide covariation and base-pairing potential between bRNAs and their target (top) and donor (bottom) sequences, calculated from 5,511 bRNA–target pairs and 2,201 bRNA–donor pairs, as described previously². The IS621 bRNA sequence is shown across the x-axis. Covariation scores calculated from thousands of orthologues are colored according to strand complementarity, with -1 (blue) representing high covariation and a bias toward top strand base-pairing, 1 (red) representing high covariation and a bias toward bottom strand base-pairing, and 0 indicating

no detectable covariation. Regions with substantial covariation signals indicating base-pairing for IS621 are boxed. These data indicated base-pairing potential between TBL-HSG P81 and dDNA P7 (red arrow) and DBL-HSG P166 and tDNA P7 (orange arrow) in IS621, suggesting the functional importance of the base-pairing at these positions across the IS110 orthologues. HSG, handshake guide. (b) Schematic of the predicted TBL–tDNA and DBL–dDNA base-pairing patterns before and after the strand exchange.

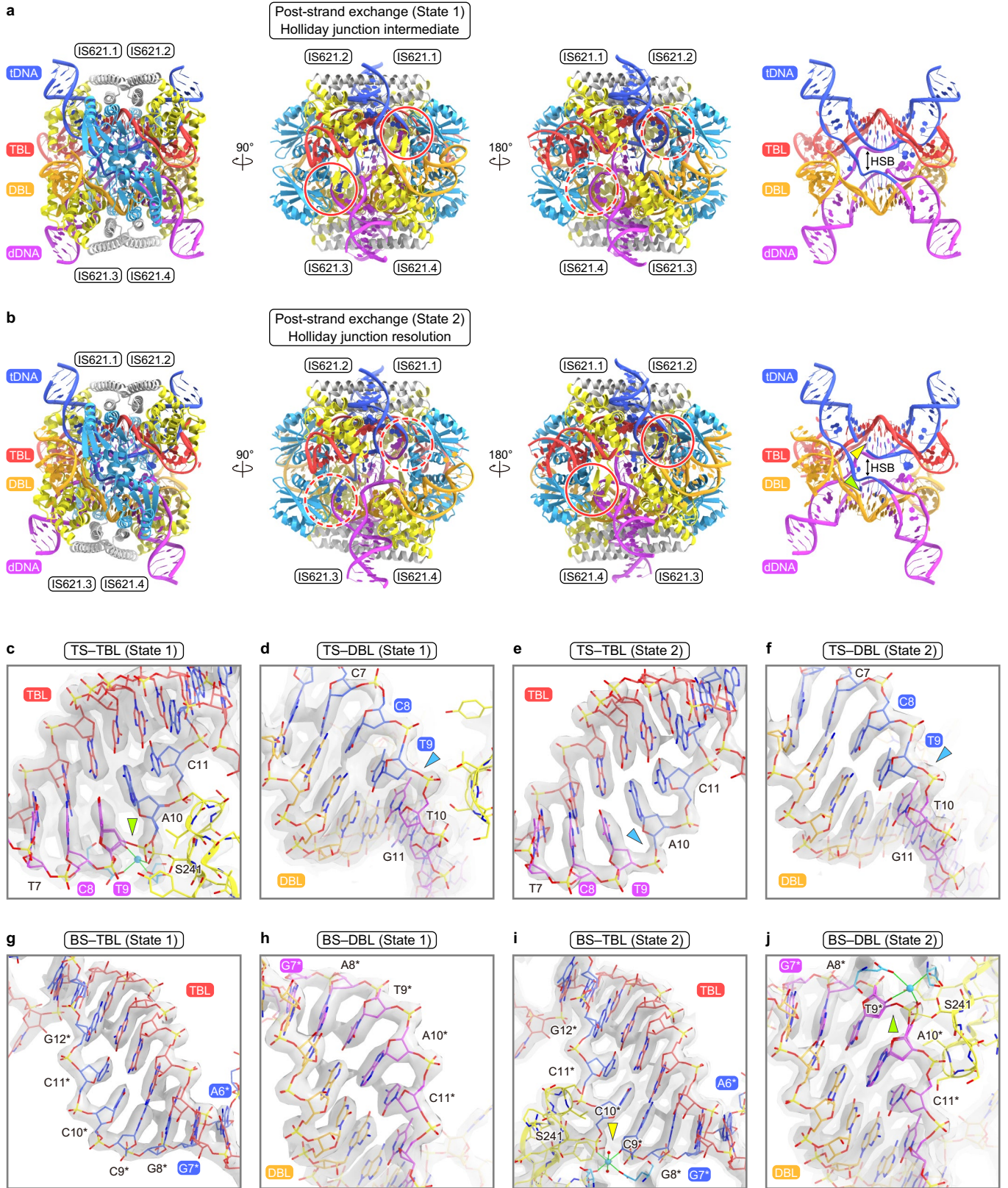


Extended Data Fig. 8 | See next page for caption.

Extended Data Fig. 8 | Effects of handshake base-pairing. (a) Schematics of the TBL/DBL and tDNA/dDNA sequences used for cryo-EM analysis and in vitro recombination assays. The pre- and post-HSB (handshake base-pairing) bRNAs stabilize the synaptic complex in the pre- and post-strand exchange states, respectively. Mutated nucleotides in the pre- and post-HSB bRNAs and their complementary DNA nucleotides are highlighted. (b) Effects of handshake base-pairing on in vitro DNA activity of IS621. Three bRNAs with different HSGs, A81/U82/G166/U167 (WT), G81/C82/A166/U167 (pre-HSB) or A81/U82/G166/C167 (post-HSB), were used for the in vitro DNA recombination experiments. The tDNA (38 bp) and dDNA (44 bp) substrates were labeled with Cy5 and FAM at the 5' ends of the top and bottom strands, respectively. The Cy5/FAM-tDNA (38 bp) and Cy5/FAM-dDNA (44 bp) were mixed with the

non-labeled dDNA (100 bp) and tDNA (102 bp), respectively. The DNA substrates were incubated with the IS621-bRNA complex at 37 °C for 1 h, and the reaction was then analyzed using an 18% TBE-urea gel. Recombination between the Cy5/FAM-dDNA and tDNA and between the Cy5/FAM-tDNA and dDNA yields 60- and 69-bp Cy5-labeled products, respectively. For the results with the labeled tDNA and pre- and post-HSB bRNAs, the band intensities of the product and cleaved DNAs were quantified, and the recombination ratios (product DNA / product DNA + cleaved DNA) were calculated. Experiments were repeated at least three times with similar results. (c) Effects of handshake base-pairing between the DBL-HSG and dDNA on IS621-mediated DNA recombination in *E. coli*. Data are shown as mean \pm SD for three biological replicates.

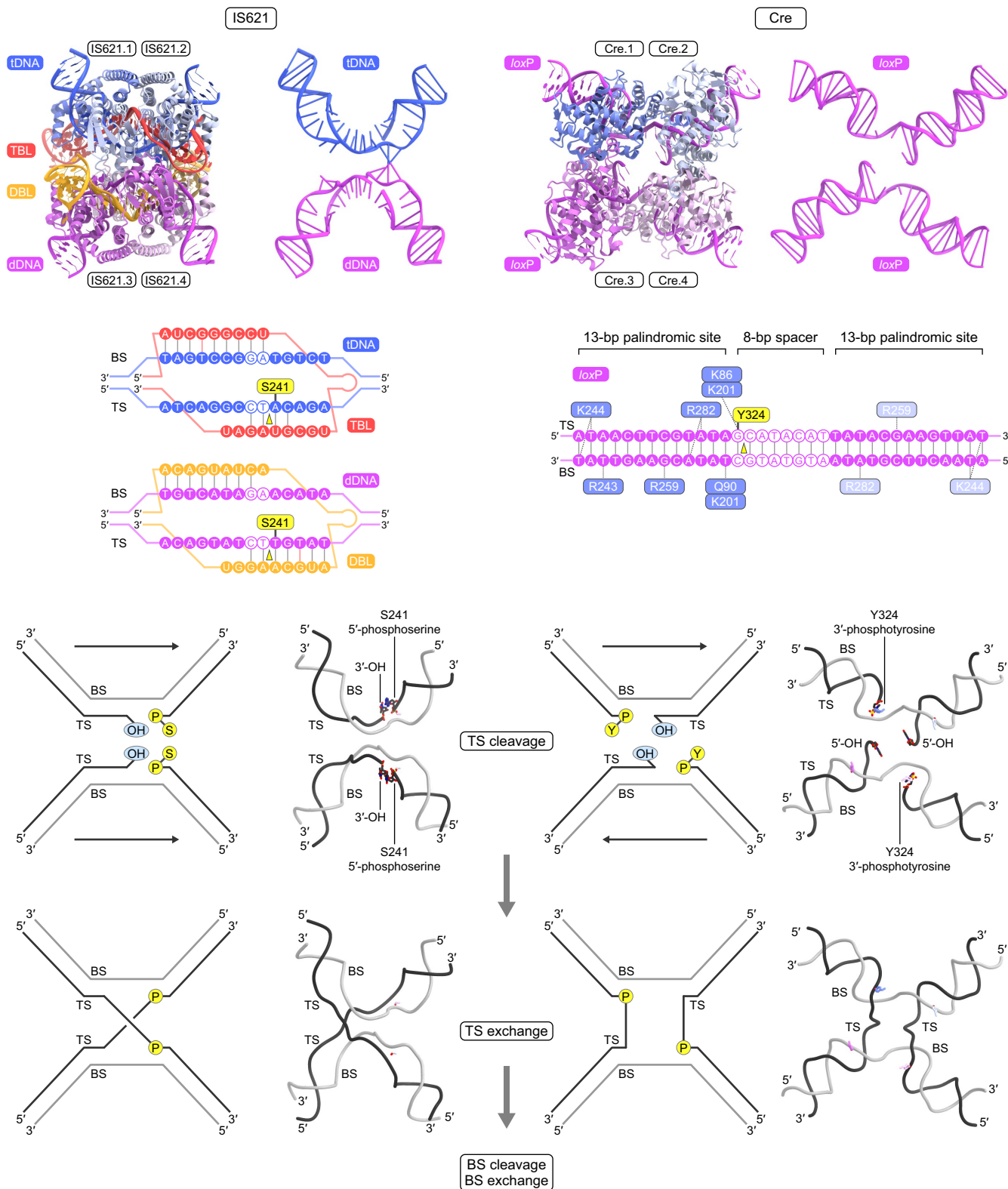
Article



Extended Data Fig. 9 | See next page for caption.

Extended Data Fig. 9 | Structures of the IS621 synaptic complexes in the post-strand exchange states. (a, b) Structures of the IS621 synaptic complexes in the post-strand exchange states (state 1) (a) and (state 2) (b). The active sites with the ordered and disordered S241 residues are indicated by red solid and dashed circles, respectively. (c–j) Close-up views of TS–TBL (state 1) (c), TS–DBL (state 1) (d), TS–TBL (state 2) (e), TS–DBL (state 2) (f), BS–TBL (state 1) (g), BS–DBL (state 1) (h), BS–TBL (state 2) (i), and BS–DBL (state 2) (j). Cryo-EM density maps are shown as grey semi-transparent surfaces. The Mg²⁺ ions are depicted as cyan spheres. In (c), (d), (i), and (j), the density maps are contoured at two different

levels. The top strand is partially religated at the RuvC.1–Tnp.4 active site in state 1 (green arrow) (c), whereas the top strand is fully religated at the RuvC.1–Tnp.4 active site in state 2 (cyan arrow) (e). The top strands are fully religated at the RuvC.3–Tnp.2 active site in states 1 and 2 (cyan arrows) (d, f). The bottom strands of tDNA and dDNA are not cleaved in state 1 (g, h). The bottom strand of tDNA is fully cleaved at the RuvC.2–Tnp.3 active site in state 2 (yellow arrow) (i), whereas that of dDNA is partially cleaved at the RuvC.4–Tnp.1 active site in state 2 (green arrow) (j). TS, top strand; BS, bottom strand.



Extended Data Fig. 10 | Comparison of IS621 and Cre. Comparison of the synaptic complex structures, DNA recognition mechanisms, and DNA recombination mechanisms between IS621 and Cre (PDB: 1CRX and 3CRX). In the recombination reactions catalysed by IS621 and Cre, the top strands in two DNA molecules are cleaved, forming covalent protein–DNA intermediates. DNA cleavage sites are indicated by yellow triangles. Note that the relative

angles between the two DNA molecules differ by -180° between the synaptic complexes of IS621 and Cre, resulting in the opposite orientations of their HJ intermediates (parallel for IS621 and antiparallel for Cre). The orientations of the two DNA molecules are indicated by arrows. TS, top strand; BS, bottom strand.

Extended Data Table 1 | Cryo-EM data collection, refinement, and validation statistics

State	Pre-strand exchange state	Pre-strand exchange locked state	Post-strand exchange state (State 1)	Post-strand exchange state (State 2)
EMDB ID	EMD-37827	EMD-37828	EMD-37829	EMD-37830
PDB ID	8WT6	8WT7	8WT8	8WT9
Data collection and processing				
Microscope	Titan Krios G3i		Titan Krios G4	
Detector	Gatan K3 Camera with Quantum LS energy filter			
Magnification	105,000			
Voltage (kV)	300			
Electron exposure ($e^-/\text{\AA}^2$)	49	50		64
Defocus range (μm)	-0.8 to -2.0			-0.8 to -1.6
Pixel size ($\text{\AA}/\text{px}$)	0.83			
Symmetry imposed	C1			
Number of movies	5,586	5,499		15,572
Initial particle images	3,912,397	4,563,380		11,156,243
Final particle images	450,219	875,289	630,357	752,628
Map resolution (\AA)	2.52	2.72	2.88	2.73
FSC threshold	0.143	0.143	0.143	0.143
Model building and refinement				
Model composition				
Protein residues	1,246	1,246	1,246	1,258
RNA residues	127	127	127	127
DNA residues	106	112	112	112
Protein atoms	9,843	9,855	9,889	9,952
RNA atoms	2,718	2,691	2,691	2,691
DNA atoms	2,176	2,294	2,335	2,335
Other atoms	6	6	1	4
Average B factor (\AA^2)				
Protein	84.6	101.7	41.9	29.7
RNA	101.3	123.9	57.2	48.9
DNA	111.2	131.8	70.2	61.0
Other	72.0	94.1	36.9	29.6
R.M.S. deviations from ideal				
Bond lengths (\AA)	0.003	0.003	0.003	0.003
Bond angles ($^\circ$)	1.05	0.91	0.90	0.96
Validation				
Clashscore	0.44	0.25	0.22	0.58
Rotamer outliers (%)	0.40	0.49	0.59	0.98
Ramachandran plot				
Favored (%)	99.3	99.3	98.1	99.2
Allowed (%)	0.7	0.7	1.9	0.8
Outlier (%)	0.0	0.0	0.0	0.0

Reporting Summary

Nature Portfolio wishes to improve the reproducibility of the work that we publish. This form provides structure for consistency and transparency in reporting. For further information on Nature Portfolio policies, see our [Editorial Policies](#) and the [Editorial Policy Checklist](#).

Statistics

For all statistical analyses, confirm that the following items are present in the figure legend, table legend, main text, or Methods section.

- | | |
|-------------------------------------|--|
| n/a | Confirmed |
| <input checked="" type="checkbox"/> | <input type="checkbox"/> The exact sample size (n) for each experimental group/condition, given as a discrete number and unit of measurement |
| <input type="checkbox"/> | <input checked="" type="checkbox"/> A statement on whether measurements were taken from distinct samples or whether the same sample was measured repeatedly |
| <input checked="" type="checkbox"/> | <input type="checkbox"/> The statistical test(s) used AND whether they are one- or two-sided
<i>Only common tests should be described solely by name; describe more complex techniques in the Methods section.</i> |
| <input checked="" type="checkbox"/> | <input type="checkbox"/> A description of all covariates tested |
| <input checked="" type="checkbox"/> | <input type="checkbox"/> A description of any assumptions or corrections, such as tests of normality and adjustment for multiple comparisons |
| <input type="checkbox"/> | <input checked="" type="checkbox"/> A full description of the statistical parameters including central tendency (e.g. means) or other basic estimates (e.g. regression coefficient) AND variation (e.g. standard deviation) or associated estimates of uncertainty (e.g. confidence intervals) |
| <input checked="" type="checkbox"/> | <input type="checkbox"/> For null hypothesis testing, the test statistic (e.g. F , t , r) with confidence intervals, effect sizes, degrees of freedom and P value noted
<i>Give P values as exact values whenever suitable.</i> |
| <input checked="" type="checkbox"/> | <input type="checkbox"/> For Bayesian analysis, information on the choice of priors and Markov chain Monte Carlo settings |
| <input checked="" type="checkbox"/> | <input type="checkbox"/> For hierarchical and complex designs, identification of the appropriate level for tests and full reporting of outcomes |
| <input checked="" type="checkbox"/> | <input type="checkbox"/> Estimates of effect sizes (e.g. Cohen's d , Pearson's r), indicating how they were calculated |

Our web collection on [statistics for biologists](#) contains articles on many of the points above.

Software and code

Policy information about [availability of computer code](#)

- Data collection: EPF v3.2.0.4776
- Data analysis: cryoSPARC v4.4.0, AlphaFold2, COOT v0.9.8.93, Phenix v1.20.1, Servalcat v0.4.65, UCSF Chimera X v1.4, CueMol2 (<http://www.cuemol.org/>), GraphPad Prism 10

For manuscripts utilizing custom algorithms or software that are central to the research but not yet described in published literature, software must be made available to editors and reviewers. We strongly encourage code deposition in a community repository (e.g. GitHub). See the Nature Portfolio [guidelines for submitting code & software](#) for further information.

Data

Policy information about [availability of data](#)

All manuscripts must include a [data availability statement](#). This statement should provide the following information, where applicable:

- Accession codes, unique identifiers, or web links for publicly available datasets
- A description of any restrictions on data availability
- For clinical datasets or third party data, please ensure that the statement adheres to our [policy](#)

Cryo-EM density maps have been deposited in the Electron Microscopy Data Bank under the accession codes EMD-37827 (pre-strand exchange state), EMD-37828 (pre-strand exchange locked state), EMD-37829 (HJ intermediate state), and EMD-37830 (HJ resolution state). Atomic coordinates have been deposited in the

Protein Data Bank under IDs 8WT6 (pre-strand exchange state), 8WT7 (pre-strand exchange locked state), 8WT8 (HJ intermediate state), and 8WT9 (HJ resolution state). PDB: 7S4X, 1CRX, 3CRX, 1ZR2, and 8B4H were used for structural comparison.

Research involving human participants, their data, or biological material

Policy information about studies with [human participants or human data](#). See also policy information about [sex, gender \(identity/presentation\), and sexual orientation](#) and [race, ethnicity and racism](#).

Reporting on sex and gender	n/a
Reporting on race, ethnicity, or other socially relevant groupings	n/a
Population characteristics	n/a
Recruitment	n/a
Ethics oversight	n/a

Note that full information on the approval of the study protocol must also be provided in the manuscript.

Field-specific reporting

Please select the one below that is the best fit for your research. If you are not sure, read the appropriate sections before making your selection.

Life sciences Behavioural & social sciences Ecological, evolutionary & environmental sciences

For a reference copy of the document with all sections, see nature.com/documents/nr-reporting-summary-flat.pdf

Life sciences study design

All studies must disclose on these points even when the disclosure is negative.

Sample size	No sample size calculations were performed, as this is generally not relevant to biochemical and bacterial experiments.
Data exclusions	Damaged particles were excluded during 2D and 3D classification in cryo-EM reconstitution to obtain high-resolution structures, according to the standard procedures in single-particle cryo-EM analysis.
Replication	All functional experiments were performed with independent replicates, according to widely adopted protocols in the field (three technical or biological replicates). Biochemical and bacterial experiments were performed with at least three technical and biological replicates, respectively.
Randomization	No randomization was performed. Randomization is not relevant to this study, as human subjects or live animals were not involved.
Blinding	No blinding was performed. Blinding is not relevant to this study, as human subjects or live animals were not involved.

Reporting for specific materials, systems and methods

We require information from authors about some types of materials, experimental systems and methods used in many studies. Here, indicate whether each material, system or method listed is relevant to your study. If you are not sure if a list item applies to your research, read the appropriate section before selecting a response.

Materials & experimental systems

n/a	Involved in the study
<input checked="" type="checkbox"/>	<input type="checkbox"/> Antibodies
<input type="checkbox"/>	<input checked="" type="checkbox"/> Eukaryotic cell lines
<input checked="" type="checkbox"/>	<input type="checkbox"/> Palaeontology and archaeology
<input checked="" type="checkbox"/>	<input type="checkbox"/> Animals and other organisms
<input checked="" type="checkbox"/>	<input type="checkbox"/> Clinical data
<input checked="" type="checkbox"/>	<input type="checkbox"/> Dual use research of concern
<input checked="" type="checkbox"/>	<input type="checkbox"/> Plants

Methods

n/a	Involved in the study
<input checked="" type="checkbox"/>	<input type="checkbox"/> ChIP-seq
<input type="checkbox"/>	<input checked="" type="checkbox"/> Flow cytometry
<input checked="" type="checkbox"/>	<input type="checkbox"/> MRI-based neuroimaging

Eukaryotic cell lines

Policy information about [cell lines and Sex and Gender in Research](#)

Cell line source(s)	Thermo Fisher Scientific
Authentication	<i>Describe the authentication procedures for each cell line used OR declare that none of the cell lines used were authenticated.</i>
Mycoplasma contamination	<i>Confirm that all cell lines tested negative for mycoplasma contamination OR describe the results of the testing for mycoplasma contamination OR declare that the cell lines were not tested for mycoplasma contamination.</i>
Commonly misidentified lines (See ICLAC register)	<i>Name any commonly misidentified cell lines used in the study and provide a rationale for their use.</i>

Plants

Seed stocks	not relevant
Novel plant genotypes	not relevant
Authentication	not relevant

Flow Cytometry

Plots

Confirm that:

- The axis labels state the marker and fluorochrome used (e.g. CD4-FITC).
- The axis scales are clearly visible. Include numbers along axes only for bottom left plot of group (a 'group' is an analysis of identical markers).
- All plots are contour plots with outliers or pseudocolor plots.
- A numerical value for number of cells or percentage (with statistics) is provided.

Methodology

Sample preparation	All cells were E. coli. Cells were scraped from agar plates, resuspended in DPBS, and diluted to the appropriate concentration.
Instrument	Agilent NovoCyte Quanteon
Software	NovoExpress software was used for flow cytometry analysis
Cell population abundance	At least 50,000 cells were analyzed.
Gating strategy	The majority (95%) of cells were gated on FSC/SSC. No further gating was performed.

- Tick this box to confirm that a figure exemplifying the gating strategy is provided in the Supplementary Information.